Quantitative Susceptibility Mapping Reproducibility with 7T Ultra-High Field MRI

Martin Rimbereid Vik

Master's thesis in applied physics and mathematics

Supervisor: Pål Erik Goa, IFY

Trondheim, October 6, 2022

Norwegian University of Science and Technology
The Faculty of Natural Sciences and Technology
Department of Physics

NTNU
Norwegian University of
Science and Technology

1 Abstract

Quantitative susceptibility mapping (QSM) has been proposed as a promising method of non-invasive in-vivo determination of spatial distribution of magnetic susceptibility. Magnetic susceptibility is a characteristic property of material and biological tissue which can give insight into chemical and molecular composition. Elevated concentration of iron in the brain have been linked to various neurological disease such as Parkinsons disease [1] and multiple sclerosis [2]. Tissues with elevated concentrations of iron have paramagnetic properties. Hence, accumulation of brain iron can be linked to elevated susceptibility of the corresponding tissue. The motivation of developing robust QSM algorithms is to propose QSM as a relighable non-invasive method of assessment of this important physical quantity using MRI data.

The construction of a QSM image involves three main steps; total field recovery (also called phase unwrapping), background field removal and dipole inversion. Total field recovery calulates the observed total field based on the MRI phase data. Background field removal isolates the tissue specific contribution to the total field creating a local field map. The final step, dipole inversion, calculates the bulk magnetic susceptibility distribution from the local field map by solving an ill-posed inversion problem.

The purpose of this thesis is to study how reliably QSM images can be reproduced, with respect to intra- and intersubject variations. A total of 27 multi gradient echo (mGRE) MRI datasets were acquired from 9 healthy voluteers at the 7T MRI lab at St. Olav in Trondheim. Each of the volunteers were scanned three times. Two of these scans were performed back-to-back and the third scan were performed after a repositioning of the voluneer in the scanner and a reshimming of the magnetic field in the scanner. An additional MP2RAGE image sequence was aquired from each volunteer, which where used for image segmentation.

A total of 81 QSM images where produced from the 27 mGRE datasets using three different QSM construction pipelines. The three diffent pipelines uses different dipole inversion algorithms to determine the magnetic susceptibility. The algorithms used were morphology enabled dipole invertion (MEDI), total generalised variation (TGV) and thresholded k-space division (TKD).

An automated atlas-based segmentation tool was used to aquire segmentations of 10 different regions of interest (ROI), representing different types of brain tissues. The segmented tissues were the thalamus, caudate nucleus, putamen, hippocampus and globus pallidus for both left- and right-hand-side of the brain. Each set of segmentation where produsedfrom T1-weighted MP2RAGE data. The segmentations were subsequently coregistered to each mGRE dataset, giving 27 unique segmentation sets. The mean QSM values from these segmentations were used to study the reproducibility of QSM images, resulting in 810 comparable datapoints.

The mean QSM values measured in this study showed a significant systematic underestimation of mean susceptibility in all ROI compared to current litterature values

of the magnetic susceptibility of equivalent brain tissue. This is suspected to be a result of the chosen method of setting the magnetic susceotibility referance value, as the underestimation where present in QSM images produced by all three pipelines.

In regards to reproducibility to intersubject variations have the most prominent effect on the reproducibility of QSM images. The intersubject variation was, on average, about tree times larger than the intrasubject variations. Further more, there was observed a varying degrees of intrasubject variations among the scanned subjects. Larger variations were linked to lower quality in the raw data and inconsistant segmentation by automated segmentation algorithms.

Scan-rescan studies showed very little variation in the measured QSM values. Reshimming of the scanner with reposition of the subject show no significant effect, compared to the scans which were performed back-to-back.

From the three different QSM algorithms, only TKD stood out. The TKD pipeline showed a systematic underestimation of magnetic susceptibility.

The study conludes that there is a need of more robust reproducable methods of QSM segmentation. The reproducitivity of the segments is arguably just as important as the the reproducibility of the QSM images themselves, as the ability to compare QSM images are dependent on the quality of the segmentations. These methods should be developed with 7T data in order preserve the high spatial resolution ultra-high field MRI provide.

Contents

1 Abstract

2 Introduction **2**

3 Theory **3**

3.1 Magnetic susceptibility in biological tissue 3

3.2 Gradient echo and multi-gradient echo images 3

3.3 MP2RAGE 5

3.4 Quantitative Suseptibility Mapping 6

3.4.1 Total field recovery 7

3.4.2 Background Field Removal 7

3.4.3 Dipole invertion 8

3.4.4 Morphology enabled dipole invertion 8

3.4.5 MEDI+0 9

3.5 Thresholded k-space division 10

3.6 Total Generalized Variation 11

4 Material and Methods **13**

4.1 Data acquisition 13

4.2 QSM acquisition 13

4.2.1 SEPIA QSM 14

4.2.2 Sepia pre-QSM prosessing 14

4.2.3 SEPIA: pre-dipole inversion 14

4.2.4 SEPIA: MEDI Dipole inversion 14

4.2.5 Sepia: TKD Dipole inversion 14

4.3 TGV 15

4.3.1 TGV: Pre-QSM processing 15

4.3.2 TGV: QSM production 16

4.4 QSM weights 17

4.4.1 Sepia weights 17

4.4.2 TGV weighting 18

4.5 Data segmentation 19
4.6 Segment refinement and statistics 20

5 Results **24**
5.1 Exclusion of volunteers 24
5.2 QSM images 24
5.3 Image Segmentation 25
5.4 Variation across different regions of interest 26
5.5 Intersubject variation 30
5.6 Intrasubject variation 32
5.7 Variation between different pipelines 33

6 Discussion **35**
6.1 QSM image quality 35
6.1.1 Differances in brain masking 35
6.2 Intrasubject variation 36
6.2.1 Effect of repositioning of volunteers and reshimming of scanner 36
6.3 Intersubject variation 36
6.4 Variation between different pipelines 37
6.5 ROI specific susceptibility variations 38
6.6 Choice of referance region 40
6.7 Segmentation and coregistration 40
6.8 QSM weights 42
6.9 Further work 43

7 Conclusion **44**

2 Introduction

Magnetic susceptibility is a physical quantity that describes the change in magnetization of a material in response to an applied magnetic field. The magnetic susceptibility is considered as an important source of image contrast in magnetic resonance imaging (MRI). The property has long been considered as a nuisance rather than a benefit, as interfaces with big susceptibilitiesare known to cause long-ranging field distortions in MRI. However, with the development of ultra-high field MRI scanners have magnetic susceptibility been increasingly considered as a source of quantitative tissue information in vivo. Ultra-high field scanners utilize higher field strengths ($>$ 3 Tesla), which can potentially provide higher spatial resolution compared to conventional clinical MRI scanners.

Since the earliest days of MRI, the quantification of magnetic susceptibility was considered to be an important goal, as it was anticipated that magnetic susceptibility could be useful to characterize diseased tissue. Iron has in the last century been considered an essential trace element involved in a variety of biological mechanisms in the human body. Disturbances of iron concentrations in tissue have been linked to several degenerative diseases, which have raised strong interest in non-invasive iron mapping techniques [3]. Hence, in later years, work has been undertaken to quantify non-invasively magnetic susceptibility distributions with MRI. A method of obtaining such magnetic susceptibility distributions is quantitative susceptibility mapping, QSM.

Obtaining QSM images are produced from high resolution T2*-weighted MRI images, where the signal phase is strongly related to local magnetic field changes. The computing process of QSM involves several essential steps. First the raw signal phase is unwrapped. Subsequently are magnetic field contribution from regions outside the tissue of interest are removed, leaving a map of local magnetic field shifts. The final step calculates the magnetic susceptibility distribution utilizing relations between local field perturbation and the underlying tissue magnetic susceptibility distribution. This final step, called dipole inversion, involves solving an ill-posed inverse problem.

In this study we wanted to study the reproducibility aspect of constructing QSM data from multi-gradient echo MRI data acquired from a 7T MRI scanner at St. Olavs hospital in Trondheim.

3 Theory

3.1 Magnetic susceptibility in biological tissue

Magnetic susceptibility, χ, refers to the magnetizability of a material when placed in a magnetic field B_0. Magnetic susceptibility describes the proportionality between the material's macroscopic magnetization M and local magnetic field B, ($M = \chi\frac{B_0}{\mu_0}$), where μ_0 is the magnetic permeability in a vacuum. A material's magnetic susceptibility is dependent on its molecular constituents, and originates from spins and motions of nuclei and their electrons. The susceptibility can be positive or negative, reflecting whether magnetization aligns with the field (paramagnetism) or opposes it (diamagnetism). Paramagnetism generally originates from field-induced alignment of unpaired electron spins, whereas diamagnetism is associated with field-induced alteration of electron orbits [4].

Human brain tissues have a rather weak (diamagnetic) magnetic susceptibility that is dominated by that of water ($\chi = 9.05$ ppm) because of its large abundance. Across the gray (GM) and white (WM) matter of healthy brain, it varies within a range from about 9.2 to 8.8 ppm. This variation is primarily caused by variations in iron and myelin content, which both have a concentration and susceptibility sufficiently different from those of water. The lipids in myelin are diamagnetic (relative to water) and, as a result, heavily myelinated WM is generally the most diamagnetic tissue in healthy brain. Somewhat outside the range for χ mentioned above is blood inside the venous vasculature, where iron in deoxyhemoglobin renders the susceptibility slightly more paramagnetic (fully deoxygenated blood: $\chi = \sim 7.9$ ppm). A wider range for magnetic susceptibilities may also be found under pathological conditions. For example, calcifications may result in a more diamagnetic susceptibility, whereas the accumulation of iron (associated with neurodegeneration or as a result of microbleeds) may render the susceptiblity more paramagnetic [3] [5].

3.2 Gradient echo and multi-gradient echo images

In priciple can any MR sequence accruing phase information during the data acquisition be utilized to monitor field variations. However, contributions to the local resonance frequency caused by chemical shift effects, which depend on the specific molecular environment of the nucleus, are especially of interest. These chemical shifts are often imaged using T2-weighted MRI sequences. T2 is defined as a time constant for the transverse magnetization decay arising from natural interactions at the atomic or molecular level. T2 can be used as a measurement of those processes contributing to the transverse decay of the MR signal that arise from natural interactions at the atomic and molecular levels within the tissue of interest. The transverse magnetization does however decay much faster in vivo than would be predicted by natural atomic and molecular mechanisms; this observed rate is denoted

T2*. T2* is primarily a result of inhomogeneities in the main magnetic field, and T2* is always less than or equal to T2 [6].

Certain MR sequences are considered particularly useful to image local magnetic homogeneity effects. Gradient echo (GRE) sequences are among these squences. GRE images is produced by a single RF pulse in conjunction with a gradient reversal. Following the RF pulse, the first negative-going lobe of the gradient causes a phase dispersion of the precessing spins. When this gradient is reversed, the spins refocus and form a gradient (recalled) echo. The phase shifts observed in GRE images result from magnetic field inhomogeneities, static tissue susceptibility gradients, or chemical shifts are not cancelled at the center of the GRE. Image contrast is therefore dictated not by true T2-relaxation, but by these other factors which constitute T2*. This makes GRE particularly suited for QSM [7].

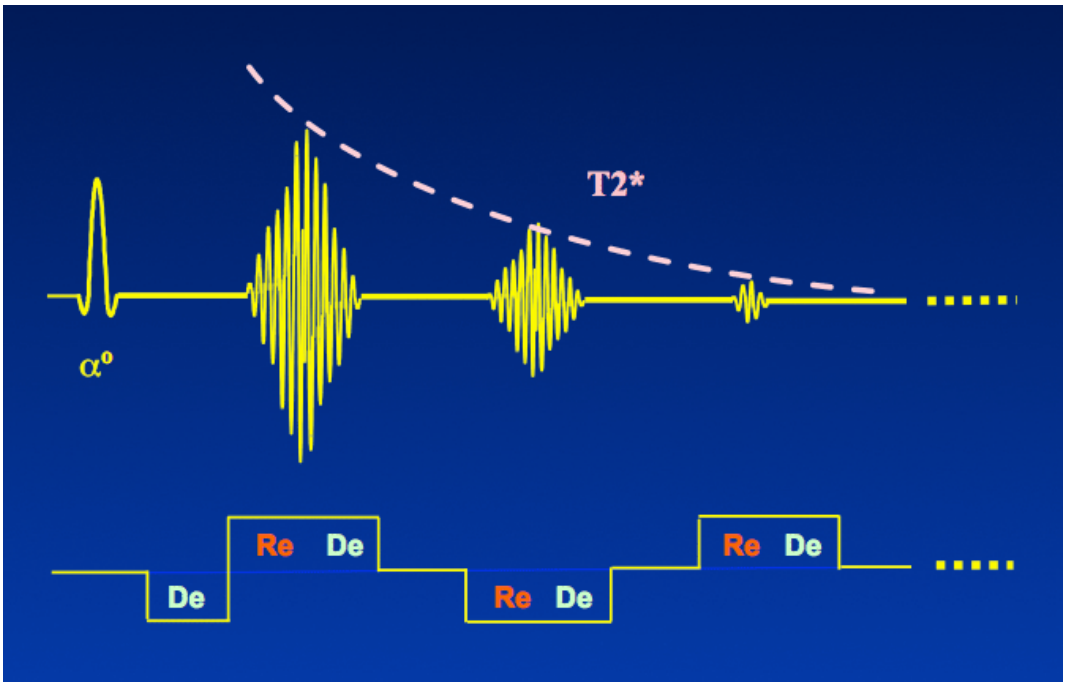

Figure 1: A schematic of a multi-echo GRE sequence. The first half of the larger gradient lobes rephase (Re) the signal. The last half dephases (De). Each subsequent echo is smaller than the last. Obtained from MRIquestions [7].

The associated phase maps of GRE data containing $\phi(\vec{r})$, or, equivalently, frequency maps $\Delta f(\vec{r})$ reflect the sample magnetization and thus its magnetic susceptibility. The GRE signal phase $\phi(\vec{r}, TE)$ at echo time, TE, can be descibed by:

$$\phi(\vec{r}) = \phi_0 + 2\pi \cdot \Delta f(\vec{r}) \cdot TE = \phi_0 + \gamma \cdot \Delta B_z(\vec{r}) \cdot TE, \tag{1}$$

where ϕ_0 is a phase offset originating from the radiofrequency response of the sample. The gyromagnetic ratio of hydrogen is represented by γ. As TE is strongly influencing the sensitivity of GRE phase images to magnetic field perturbations, whilst, at the same time, deteriorating the phase signal-to-noise ratio (SNR), it has been shown that optimum phase contrast is achieved for a TE equal to the tissue's effective transverse relaxation time T2*. However, as a variety of tissue types, with different T2* values, are considered simultaneously in MRI at any given time, a single-echo acquisition cannot reflect the magnetic field variation across all tissues in an optimal manner. This issue is adressed by proposing multi-echo GRE (mGRE) sequences as the data acquisition sequence for QSM. Multi-echo GRE offers more flexibility in tailoring the T2* contrast, as data from multiple TE are available from a single aquisition. Aquisition of multiple echo times the determination of magnetic field perturbations with higher SNR. A shematic illustration of a multi-GRE sequence is illustrated in figure 1.

3.3 MP2RAGE

The MP2RAGE sequence uses two Turbo-FLASH gradient echoo readouts between each appied inversion pulse. The first inversion time (TI1) is short, producing a T1-weighted image with the gray matter nulled at the center of k-space. The second inversion time (TI2) is longer, which combined with a small flip angles $(4 - 5^\circ)$ and long repetition time (TR), produces spin-density-weighted contrast. By combining image data from the 1st and 2nd readouts, T2* and B1 inhomogeneity effects can be largely cancelled out, resulting in a strongly T1-weighted image with superior gray matter to white matter contrast [8]. The two images acquired at TI1 and TI2 are subsequently combined using the following expression:

$$\text{MP2RAGE} = \frac{\text{GRE}_{TI1} \cdot \text{GRE}_{TI1}}{\text{GRE}_{TI1} + \text{GRE}_{TI2}}. \tag{2}$$

A schematic illustration of a MP2RAGE sequence is illustrated in figure 2.

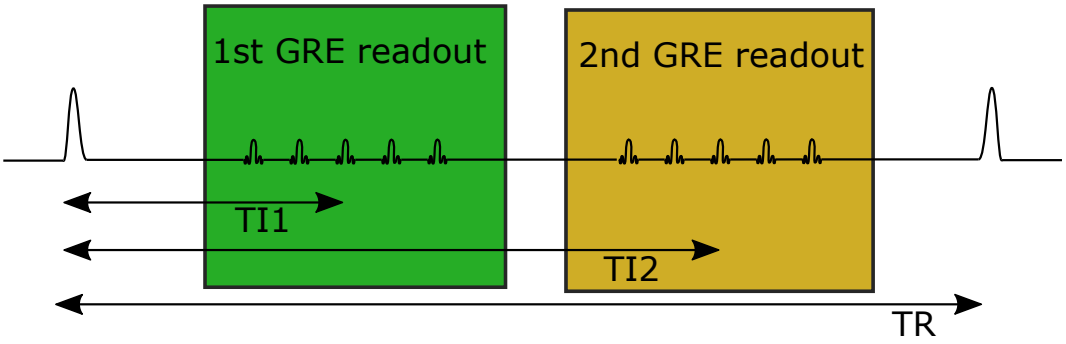

Figure 2: The QSM processing pipeline includes phase unwrapping, background field removal (requiring a mask separating background and organ of interest) and the dipole inversion.

3.4 Quantitative Suseptibility Mapping

Quantitative Suseptibility Mapping (QSM) requires multiple processing steps such as phase unwrapping, background field removal and a field-to-source dipole inversion. Current state-of-the-art techniques primarily utilize iterative optimization procedures to solve the inversionand background field correction, which are computationally expensive and require acareful choice of regularization parameters [9].

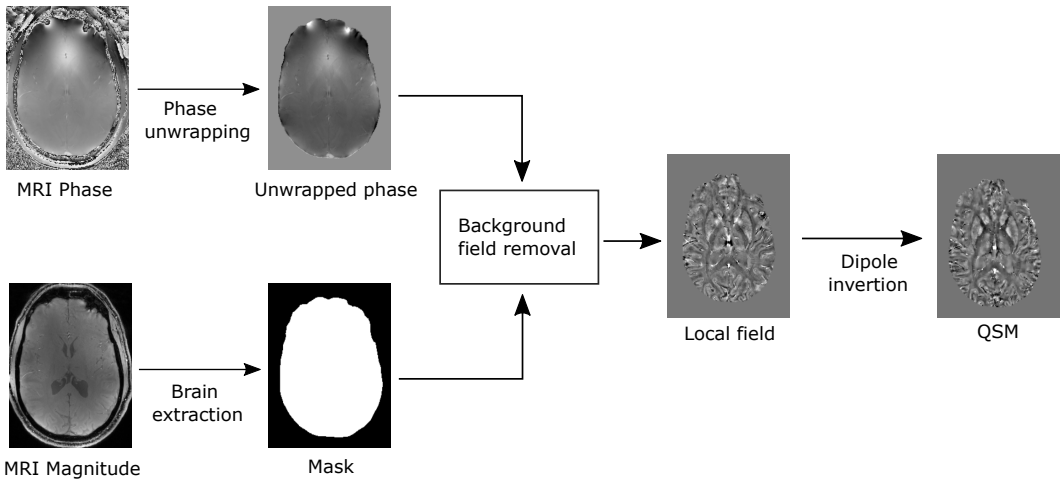

Figure 3: The QSM processing pipeline includes phase unwrapping, background field removal (requiring a mask separating background and organ of interest) and the dipole inversion.

3.4.1 Total field recovery

Total field recovery, also called phase unwrapping, strategies are necessary because MRI scanner detects signal phase values between $-\pi$ and π, leading to phase jumps (wraps) of 2 within the raw data. The true phase, $\phi(\vec{r})$ is obtained by compansating each wrap by locally adding multiples of 2π.

$$\phi(\vec{r}) = \phi_w(\vec{r}) + n(\vec{r}) \cdot 2\pi, \tag{3}$$

where ϕ_w is the wrapped phase. The true phase is then corrected by imposing temporal or spatial constraints, this proscess is commonly called phase unwrapping. There are numerous conventional techniques in use and each method results in a trade-off between speed and accuracy [9].

The result of this step is a map of the total field, including contributions from back ground fields and local field perturbations.

3.4.2 Background Field Removal

The elimination of so-called background fields is an essential step in phase MRI and QSM. Background fields, which are field contributions caused by sources outside the region/tissue of interest. These contributions are often one to two orders of magnitude stronger than tissue-related field variations from within the region of interest (ROI), hampering quantitative interpretation of field maps [10]. Common examples of such background fields can be main static magnetic field inhomogenities. Magnetic field inhomogenities can occure due to shimming coils and proximity of tissue-air interfaces etc.

There are numerous conventional methods of removing background field contributions which can be classified the base assumptions of the algorithms:

- Methods assuming no sources close to boundaries.
- Methods assuming no harmonic internal and boundary fields.
- Methods not employing an explicit boundaryassumption, but minimizing an objective function.

The background field removal step result in a map of the isolated local field shifts, only including local field perturbations originating from the tissue.

SHARP One example assuming no sources close to boundaries is sophisticated harmonic artifact reduction for phase data (SHARP) [11]. This assumtion is extended with the V-SHARP [12] method which reduces artifacts at the edges using decreasing kernel sizes towards the boundary.

3.4.3 Dipole invertion

Dipole inversion is the step in which the susceptibility distribution is derived. This is achieved, in principle, by assuming the measured local field ΔB_{local} to be a convolution of a suseptibility distribution and a unit dipole kernel;

$$\Delta B_{\text{local}}(\vec{r}) = \chi(r) * d(\vec{r}).$$

The suseptibility distribution can then be isolated by:

$$\tilde{\chi} = FT^{-1} \left\{ \frac{FT\{\Delta B_{\text{internal}}\}}{FT\{d(\vec{r}\}} \right\} \cdot B_0^{-1}. \tag{4}$$

However, the dipole kernel $d(\vec{r})$ can be zero at some orientations making the problem ill-posed.

The ill-posed dipole inversion step is traditionally overcome either by additional measurements at multiple orientations or by numerical stabilization strategies. Where the latter is most utilized.

The numerical strategies can be primarily divided into inverse filtering and iterative methods [13]. Inverse filtering solves the problem in the Fourier domain by dividing the pre-processed phase data by the unit dipole response yielding the magnetic susceptibility. However, small values in the unit dipole response result in an amplification of noise and errors, necessitating the replacement of small values by a fixed threshold. This method is known as truncated k-space division (TKD) and the results can be corrected for underestimated magnetic susceptibility.

The inverse problem can also be solved in the spatial domain by reformulating the problem as a Bayesian reconstruction with a data consistency term of the forward dipole model (ie, convolution of the dipole kernel with the susceptibility distribution) and a carefully designed regularization term, solving a least-squares problem. One example is the morphology-enabled dipole inversion (MEDI) algorithm, which utilize edge information from magnitude images input to the the applied regularization cost functions [9].

3.4.4 Morphology enabled dipole invertion

The morphology enabled dipole invertion (MEDI) method makes use of the observation that the locations of the interfaces (or edges) in the susceptibility distribution are nearly the same as those in T2* magnitude images obtained in the same acquisition, and we consider their discordance to be small. To promote this sparsity, a minimization is used that penalizes susceptibility at those voxels that are not

part of an interface in the magnitude image. The minimization is constrained by data fidelity ensuring that the local field induced by the estimated susceptibility distribution agrees with the local field as measured from the phase image [14].

This minimization problem can be descibed by:

$$\tilde{\chi} = \min_{\chi} \frac{1}{2}||w(e^{-if} - e^{-i(d*\chi)})||_2^2 + \lambda_1 R(\tilde{\chi}) \tag{5}$$

where $\tilde{\chi}$ is the estimated susceptibility map, $*$ the convolution operator, w is a diagonal weighting function to account for spatially varying noise levels, f is the measured local field, ∇ the gradient operator, λ_1 is a tunable regularization parameter and $R(\tilde{\chi})$ describes a functional constraint term) to impose prior knowledge onto the solution. Prior information may be derived from magnitude and phasemaps [15] by assuming that they have similar edges to the underlying brain structure [16]. The dipole kernel, d, that can be defined in both Fourier and spatial domains:

$$d = FT\left[\frac{1}{3} - \frac{k_z^2}{K^2}\right] = \frac{1}{4\pi}\frac{3\cos^2(\theta) - 1}{r^3} \tag{6}$$

where r is the magnitude of position vector $\vec{r}$ from the dipole source to the field observer, k is the magnitude of the corresponding Fourier vector $\vec{k}$ in k-space. k_z is the component of $\vec{k}$ along the B0 direction, and θ is the angle between $\vec{r}$ and the B_0 direction.

3.4.5 MEDI+0

MEDI+0 [17] proposes an automated procedure to determine a mask of the lateral ventricular cerebral spinal fluid (CSF), This CSF mask, M_{CSF}, is obtained from the brain region of interest mask, M_{brain}, by taking advantage of the characteristically low T_2^* values of CSF and by imposing connectivity in the region. This procedure adds a third term to the problem in equation 5;

$$\chi* = \min_{\chi} \frac{1}{2}||w(e^{-if} - e^{-i(d*\chi)})||_2^2 + \lambda_1||M_{\text{brain}}\nabla\chi||_1 + \lambda_2||M_{\text{CSF}}(\chi - \chi_{\bar{\text{CSF}}})||_2^2 \tag{7}$$

The implementation for automated generation of M_{CSF} and setting mean susceptibility of CSF as referance:

1. Threshold T_2^* image:$T_2^* \triangleq < R$, for a given threshold R.
2. Define brain centroid, $\mathrm{c} = \frac{1}{N}\sum_{r \subset M} r$, where N is the number of voxels in M.
3. Define central brain region: $M_C \triangleq \{r | ||r - c||_2 < 3\,\mathrm{cm}\}$
4. Analyze connectivity in $M_C \cup M_{T_2^*}$: Divide $M_C \cup M_{T_2^*}$ into connected components M_{ci} (6-neighbour) and merge the largest three components: $M_{C\mathrm{CSF}} \triangleq \{M_{C1} \cup M_{C3}\}$
5. Analyse Connectivity in R_2^*: Divide R_2^* into connected components M_i (6-neighbour) and merge all components that overlap with $M_{C\mathrm{CSF}}$: $M_{c\mathrm{CSF}} \triangleq \{\cup M_i | M_i \cap M_{c\mathrm{CSF}}\}$
6. The problem in equation 7 is solved using a Gauss-Newton conjugate gradient.
7. Finaly, $\chi_{\bar{C}\mathrm{SF}}$, measured in the produced QSM map using $M_{C\mathrm{CSF}}$, is subtracted from the entire map for zero referencing.

M_{CSF} is constructed only from threshholding T_2^* magnitude images, and is constucted independently of the QSM pipeline.

3.5 Thresholded k-space division

A very time-efficient QSM technique involve solving equation 4 directly in the Fourier domain by applying a modified dipole kernel. Thresholded k-space division (TKD) utilizes this approach to dipole inversion. In this method are a modified dipole kernel, $d'_z(\delta, \vec{k})$, replaced by a constant value at orientations where the dipole kernel in equation 6 reaches low absolute values. The modified dipole kernel can be described by:

$$\mathrm{d'}_z(\delta, \vec{k}) = \begin{cases} \frac{1}{3} - \frac{k_z}{|\vec{k}|^2} & ,\text{when } \left|\frac{1}{3} - \frac{k_z}{|\vec{k}|^2}\right| > \delta \\ \mathrm{sign}\left(\frac{1}{3} - \frac{k_z}{|\vec{k}|^2}\right) \cdot \delta & \text{otherwise} \end{cases}$$

Here, 'sign' represents the sign function. TKD is appealing because of its numerical simplicity, and has been shown to effectively limit noise amplification in the vicinity of problematic orientations. A threshold parameter, δ, in the range 0.2–0.5

are proposed to effectively reduce both streaking artifacts and noise amplification, but that systematic underestimation of magnetic susceptibility values occurs with increasing δ. The latter can be explained by the systematic inversion error in the subdomain of the Fourier space, where the dipole kernel has been modified, and can be overcome by introducing a scalar correction factor $c_\chi(\delta)$ depending on the chosen threshold [16] [18]:

$$\tilde{\chi} = FT^{-1}\left\{\frac{FT\{\Delta B_{\text{internal}}\}}{d'_z(\delta;\vec{k})\cdot c_\chi(\delta)}\right\}\cdot B_0^{-1} \tag{8}$$

3.6 Total Generalized Variation

Dipole inversion methods using total general variation (TGV) penalty have been proposed to reconstruct the underlying magnetic susceptibility distribution from gradient echo phase data.

TGV is a the semi-norm on a Banach space. Hence reconstruction problems with TGV penalty can be solved with tools developed for convex optimization problems. The TGV functional (here defined as second order TGV^2) represents a minimization problem [19]:

$$TGV^2_{\alpha_1,\alpha_0} = \min_w \alpha_1||\nabla\chi - w||_M + \alpha_0||\epsilon w||_M \tag{9}$$

Minimization is performed over all vector fields w, where ϵ denotes a symmetrized derivative for vector fields resulting in second-order symmetric tensor fields, $\epsilon w = \frac{1}{2}(\Delta w + \Delta w^T)$. For example, the symmetrized derivative ϵ for the 2 dimensional case is defined as:

$$w = \begin{pmatrix} w_1 \\ w_2 \end{pmatrix}, \epsilon w = \begin{pmatrix} \frac{\partial w_1}{\partial x} & \frac{1}{2}\left(\frac{\partial w_1}{\partial x} + \frac{\partial w_2}{\partial x}\right) \\ \frac{1}{2}\left(\frac{\partial w_1}{\partial x} + \frac{\partial w_2}{\partial x}\right) & \frac{\partial w_2}{\partial x} \end{pmatrix}$$

Second-order TGV^2 inherently balances locally the first and the second derivative of a function, as determined by the ratio of the weights α_1 and α_0.

As QSM reconstruction usually involves multiple steps, such as phase unwrapping and backgroundfield removal. This can allow errors to propagate in each step to an increasing degree. The TGV approach the wrapped phase data directly and incorporates the background field removal by introducing an auxiliary variable in the iterative regularization process for the dipole inversion.

QSM maps are recovered from the wrapped phase of single gradient echo data ϕ_{wrapped}. This recovery process is based on an optimization procedure which operates on the Laplacian Δ of the unwrapped phase ϕ. The laplacian of the wrapped phase can be described by:

$$\Delta\phi = \text{Im}\left(\Delta e^{j\phi_{\text{wrapped}}} \cdot e^{-j\phi_{\text{wrapped}}}\right). \tag{10}$$

The dipole inversion is implemented directly on the Laplacian of the phase $\Delta\phi$ by:

$$\frac{1}{3}\frac{\partial^2\chi}{\partial x^2} + \frac{1}{3}\frac{\partial^2\chi}{\partial y^2} - \frac{2}{3}\frac{\partial^2\chi}{\partial z^2} = \frac{1}{2\pi T_E \gamma B_0}\Delta\phi \tag{11}$$

The background field step was implicitly been incorporated by the introduction of an auxiliary variable ψ whose Laplacian is required to be equal to the discrepancy of this equation on the brain mask M_{brain}. This auxiliary variable is penalized by integrating its squared absolute value over M_{brain}.

The resulting inversion regularized with TGV of second order with regularization parameters (α_0, α_1) result in a variational problem:

$$\min_{\chi,\psi} \int |\psi|^2 dx \text{ subject to } \Delta\psi = \frac{1}{3}\frac{\partial^2\chi}{\partial x^2} + \frac{1}{3}\frac{\partial^2\chi}{\partial y^2} - \frac{2}{3}\frac{\partial^2\chi}{\partial z^2} - \frac{1}{2\pi T_E \gamma B_0}\Delta\phi \text{ in } \Omega \tag{12}$$

The TGV functional introduces one additional auxiliary variable in

$$TGV^2_{\alpha_1,\alpha_0}(\chi) = \min_w \alpha_1 ||\nabla\chi - w||_M + \alpha_0 ||\epsilon w||_M. \tag{13}$$

Solving this optimization problem yields susceptibility maps in a single step, without the need of separate phase unwrapping and background field fitting. This is enabled by using only the Laplacian of the unwrapped phase ($\Delta\phi$) directly in the inversion problem. The minimization with respect to ψ thus corresponds to removal of the (harmonic) background field. Minimization with respect to χ yields the TGV-regularized dipole inversion.

4 Material and Methods

4.1 Data acquisition

All data was aquired at the 7T MR lab at St. Olavs university hospital in Trondeim. In total were 12 volunteers scanned using a 7T MAGNETOM TERRA (Siemens, Munchen, Germany). Each of these individuals were scanned three times using a multi-gradient echo sequence in a single session. The first two scans were performed back to back without taking the person out of the scanner. After the first two scans was the person taken out of the scanner for a short break before the third scan. A reshimming process was performed before the third scan. A additional 0.75mm isotropic MP2RAGE scan was perfomed for each volunteer which were used for for image segmentation.

In every scan session was a main field (B0) shimming was performed using the vendors' default B0-shimming routines. B1-calibration was performed initially using the vendor's default adjustment scans.

Multi-echo 0.75mm isotropic resolution T2*-weighted GE data were acquired with: TE1/TR=2,54/31ms; 4 echoes with monopolar gradient readouts; echo-spacing = 4.7 ms; FA= 12°; bandwidth = 300 Hz/px; FoV = 23 cm, 224 axial slices, scan-time 9min.

MP2RAGE sequences were performed with 0.75 mm isotropic resolution (TR/TE/TI/FA = 4300 ms/1.99 ms/840 ms/5°) and a matrix size of 224 × 300 × 320 was acquired with GRAPPA coil mode.

All scans were perfomed using a 32-channel phased array-receiving coil. Coil combination of phase array channels was performed using Siemens ASPIRE algorithm [20], an algorithm implemented by the vendor.

4.2 QSM acquisition

Three QSM images were produced from data obtained from each of the three mGRE dataset fron each volunteer, creating a total of nine QSM images per volunteer.

Two QSM pipelines were performed in MATLAB [21] using the SEPIA-toolbox [22]. The SEPIA QSM pipelines used the exact same pipeline in regards to brain extraction, phase unwrapping and background field removal. A MEDI [23] [24] and TKD [18] dipole inversion were used for the dipole inversion step.

The third QSM pipeline was perfomed using TGV-QSM [19], which is a open source, python based, pipeline. This method needed more extensive pre- and post-processing.

Ahead of any data processing were all data converted from DICOM to NIfTI format using MRIcron [25] by appying the dcm2nii tool [26].

4.2.1 SEPIA QSM

4.2.2 Sepia pre-QSM prosessing

In order to process multi-gradient echo images in SEPIA all single echo T2* magnitude and phase images have to be merged into two magnitude and phase 4D nifti files. The fslmerge function in the FSL toolbox [27] were used to obtain 4D nifti files. The nifti header files also need to be merged to a single sepia-specific header MATLAB file. This was produced using the a header utility tool provided by the SEPIA toolbox. A visual representation of the SEPIA pipelines is shown in figure 4.

4.2.3 SEPIA: pre-dipole inversion

QSM images produced with MEDI and TKD dipole inversion used the same processing prior to dipole inversion. This processing included echo combination, brain extraction, phase unwrapping, back ground field removal and brain mask erosion. Echo combination was performed prior to phase unwrapping by the optimum weights [28] method in SEPIA. The Sepia toolbox have a FSL Brain Extraction Tool (BET) implementation which was used for brain extraction. This extraction was performed with a fractional threshold of 0.5 and a gradient threshold of 0.0. Phase unwrapping where performed with a Laplacian unwrapping [29] from STI Suite [30] toolbox. Background field removal was performed by using a V-SHARP algorithm from the MEDI [23] toolbox, using a variable kernel with a minimum radius of 3 and maximum radius of 10 voxels. B_1 residual removal by 4th order 3D polynomial harmonic fitting was performed at the end of the background field removal. The applied brain mask was eroded by 5 voxels at the mask edge prior to dipole inversion in order to exclude unrelighable voxels at the mask edge.

4.2.4 SEPIA: MEDI Dipole inversion

Dipole inversion using the MEDI toolbox was performed using regularisation parameter $\lambda_1 = 1000$ with signal-to-noise weighing enabled. MEDI+0 CSF zero referancing was enabled, with regularisation parameter of $\lambda_2 = 100$, which yielded a zero referanced QSM along with a separate CSF referance mask.

4.2.5 Sepia: TKD Dipole inversion

Dipole inversion using the TKD was performed using a dipole kernel threshold $\delta = 0.15$. MEDI+0 CSF zero referancing was enabled, with regularisation parameter of $\lambda_2 = 100$, which yielded a zero referanced QSM along with a separate CSF mask.

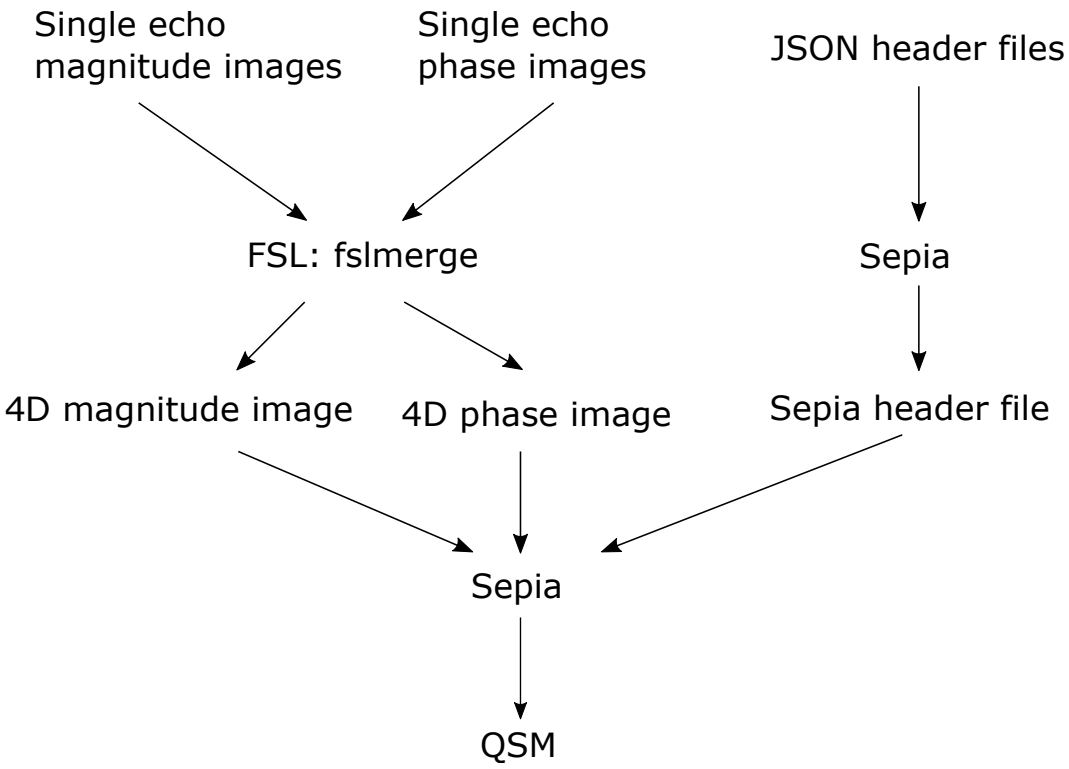

Figure 4: SEPIA QSM flowchart

4.3 TGV

Creating QSM images using TGV need some additional pre- and post-QSM-processing of the mGRE and QSM data respectively compared to the SEPIA pipelines. The preprocessing include brain extraction and rescaling of the wrapped phase data. The post-processing include combination of single echo QSM images and zero referance-ing. A visual representation of the TGV pipeline is shown in figure 5.

4.3.1 TGV: Pre-QSM processing

Brain extraction were performed using FSL BET on T2* magnitude image of the first echo in each GRE data set. BET was performed with fractional threshold of 0.5 and a gradient threshold of 0.0. This extraction was performed with robust brain center estimation enabled, which runs BET iteratively.

Phase rescaling was needed, as the TGV algorithm assumes radians$\in [-\pi, \pi]$ as a default unit for the phase image input. The aquired phase data from the Siemens 7T MAGNETOM TERRA have voxel value range of $[0, 4096]$. A simple rescaling of

the acuired data were performed directly using fslmaths in the FSLutils [27] toolbox, by;

$$\phi_{\text{rescaled phase}} = \frac{\phi_{\text{raw phase}} - 2048}{2048} \cdot \pi.$$

As a sidenote, TGV do have an implementation to rescale siemens data, but this implementation assumes that the input phase images have voxel values of $[-4096, 4096]$. This is not the case for the data aquired in this study, hence an external rescaling is needed.

4.3.2 TGV: QSM production

The TGV algorithm can not process multi echo data directly, as the algorithm only accepts a single phase image and a single brain mask as input. In order to produce a single QSM image for the total mGRE data set you need to produce a QSM image for each echo separately, resulting in four QSM images for each GRE data set. The parameters used in TGV are tabulated in table 1. The four single-echo QSM images are then combined by calculating a mean over the four QSM images, this was performed using FSLutils fslmaths.

Zero referancing was achived by using the CSF mask aquired from one of the SEPIA pipelines. The mean susceptibilty within the CSF mask are then subtracted from the QSM image matrix.

α_1	0.0015
α_2	0.0005
Number of iterations	1000
Mask erodtion	5 voxels

Table 1: Parameters used in TGV QSM.

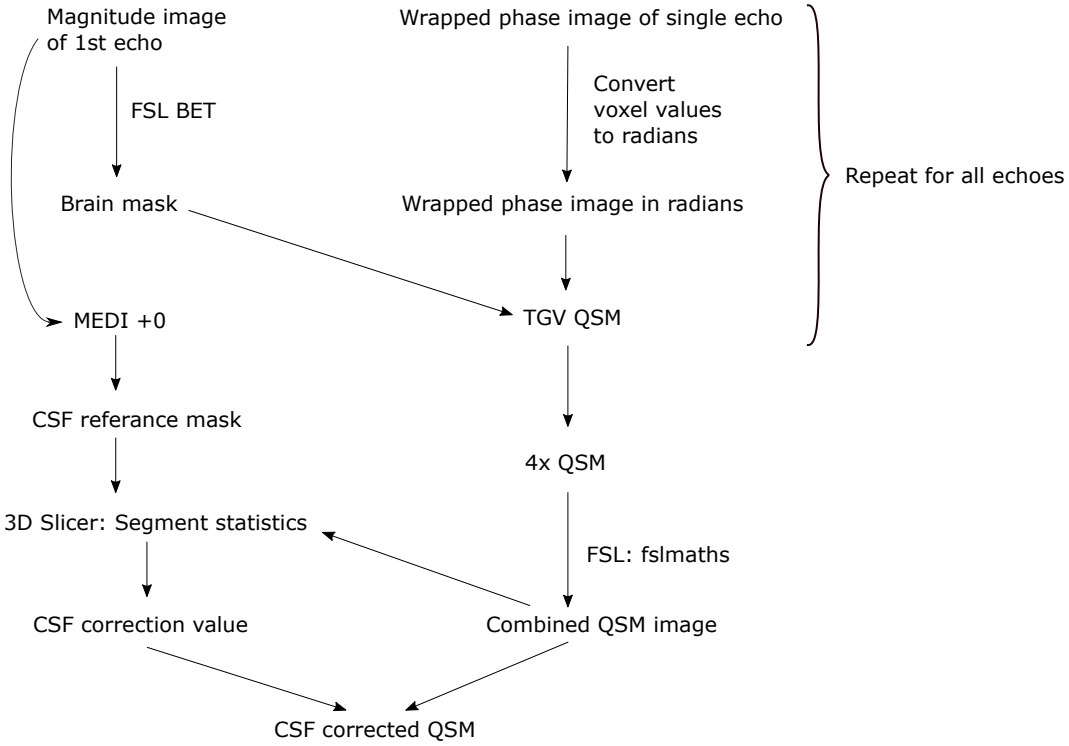

Figure 5: TGV QSM flowchart

4.4 QSM weights

4.4.1 Sepia weights

SEPIA utilises the inverse of the mapped standard deviation of the fieldmap as the weights for dipole field inversion algorithms. This is achived by the production of a weight map, which is produced by:

1. Inverting the fieldmap standard deviation and remove non-value entries (i.e., NaN & inf become 0)

$$\text{weights} = \frac{1}{SD_{\text{field map}}}$$

2. Normalisation of the weights. To establish more comparable weights between subjects and between protocols, the weights are first normalised by the value defined as (median + 3×interquartile range (IQR)). Because of the fast R2* tissues (e.g., globus pallidus), the histogram of the weights is usually negatively skewed.

$$\text{weights} = \frac{\text{weights}}{\text{median}(\text{weights}(\text{mask})) + 3 \times IQR(\text{weights}(\text{mask}))}$$

3. To avoid the weights estimated from vaious echo combination methods and dataset having significant differences in magnitude overall, the median of the histogram of the weights is re-centred to 1.

$$\text{weights} = \text{weights} - median(\text{weights}(\text{mask})) + 1$$

4. The last step is to reduce the extreme values on the right hand side of the histogram, which can introduce an overall weight offset between different echo combination methods if the dipole field inversion methods performs weight normalisation using the maximum value of the input data. Since the weights are commonly derived from the magnitude data, these extreme values often correspond to the fresh spins in the arteries and spatially sparse. To reduce the extreme values while preserving the smoothness of the weighting map, the weighting map is thresholded (threshold defined as median + 3IQR) and the extreme values are replaced by a 3x3x3 (voxel) box filtered copy:

$$\text{weights}(\text{weights} > \text{threshold}) = \text{weights}_{\text{smooth}}(\text{weights} > \text{threshold}),$$

where

$$\text{weights}_{\text{smooth}} = smooth3(\text{weight.} * \text{mask}).$$

This is the final output of the weights. Since the median after normalisation will be less than 1. Therefore, the minimum value of the weights will not be equal to zero, roughly speaking, most gray matter and white matter could have weight 1; globus pallidus, red nucleus and substantia nigra 0.7-0.9; veneous structures 0.3-0.6.

4.4.2 TGV weighting

The TGV pipeline does not produce a QSM weight map, but the QSM images are scaled at the very end of the pipeline by:

$$\text{QSM}_{TE,\text{scaled}} = \frac{\text{QSM}_{\text{TGV}}(\phi_{\text{laplace filtered}}, \text{binary mask}, \alpha_{1,2})}{2\pi \cdot TE \cdot \text{fieldstrength} \cdot \gamma}.$$

Where $\mathrm{QSM}_{\mathrm{TGV}}(\phi_{\text{laplace filtered}}, \text{binary mask}, \alpha_{1,2})$ is the calculated QSM image, TE is the echo time in seconds γ is the gyro-magnetic ratio of hydrogen.

4.5 Data segmentation

The image segmentation where performed using FSL FIRST [31]. FSL FIRST is a model-based segmentation/registration tool. The models used in FIRST are constructed from manually segmented images provided by the Center for Morphometric Analysis, MGH, Boston. The manual labels are parameterized as surface meshes and modelled as a point distribution model. Deformable surfaces are used to automatically parameterize volumetric labels in terms of meshes; these deformable surfaces are constrained to preserve vertex correspondence across the training data. Furthermore, normalized intensities along the surface normals are sampled and modelled. The shape and appearance model is based on multivariate Gaussian assumptions. Shape is then expressed as a mean with modes of variation (principal components). FIRST searches through linear combinations of shape modes of variation for the most probable shape instance given the observed intensities in a T1-weighted image.

In this study used T1-weighted images from MP2RAGE data from each volunteer to perform the segmentation. A total of 10 segmentations were considered. The considered segmented tissues included the thalamus, caudate nucleus, putamen, pallidum and hippocampus on left- and right-hand side. A 3D-visualisation of an aquired set of segmentations can be seen in figure 6.

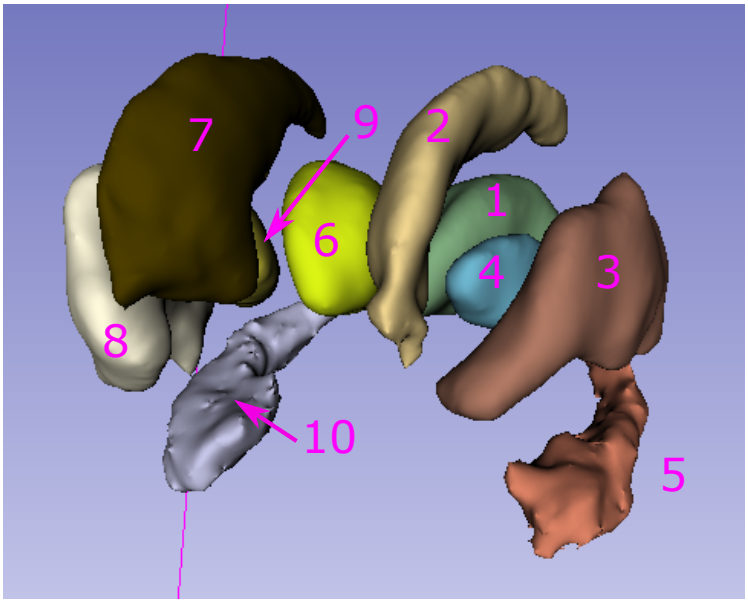

Figure 6: 3D closed surface reconstruction of segmentations aquired using FSL FIRST with a T1 weighted MP2RAGE image. The image shows segments of thalamus(1, 6), caudate nucleus(2, 7), putamen(3, 8), pallidum(4, 9) and hippocampus(5, 100) . Illustrated using 3D Slicer [32].

Not all T1-weighted images could be brain extracted directly using FSL BET directly. The spin-density-weighted MP2RAGE image was brain extracted instead to produce a brain mask for the T1 image, which proved to be more consistant.

The brain extracted spin-density-weighted image were coregistated to the T2* magnitude image of the first echo of each mGRE dataset using FSL FLIRT [33] [34] [35] using a rigid body transform with 12 degrees of freedom and trilinear iterpolation. One output file from FSL FLIRT is a transform matrix file. This transform matrix was applied to the set of segmentations obtained from T1-weighted MP2RAGE image. The end result of this process is a set of segmentations coregistered to each aquired mGRE dataset. This was repeated for all GRE data sets, resulting in a total of 27 sets of segmentations. A visual representation of the segmentation process is shown in figure 8.

4.6 Segment refinement and statistics

Some alterations were needed to the coregistered segmentations. The iterpolation method performed by the coregistration algorithm created some mislabeled islands on the surface of each segment, as can be seen in figure 7. These islands are very small compared to the total volume of the ROI. Most of these can be removed by excluding all stuctures with less than 300 voxels. This was done using the segment

editor tool in 3D-Slicer [32].

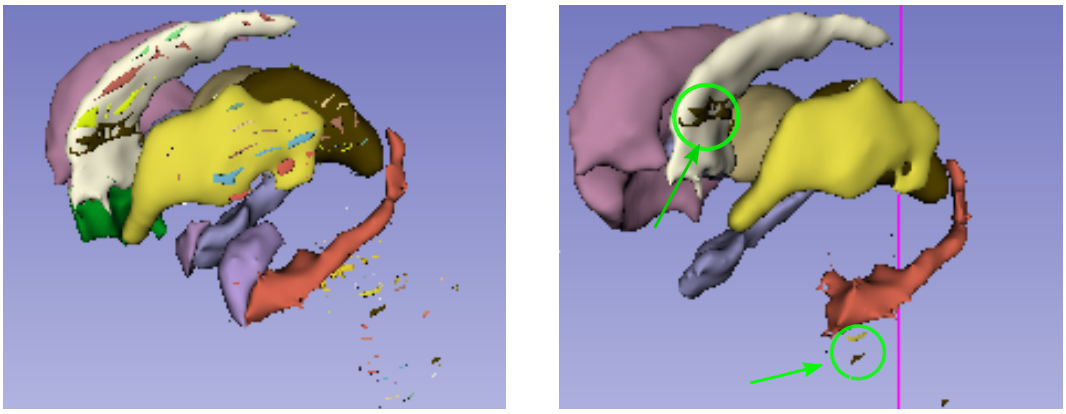

Figure 7: Left-hand side show the segmentations in figure 6 after coregistration to a T2* image using FSL FLIRT. Image on the right-hand side show the same set of segmentations after filtering in 3D Slicer. The areas highlighted on the right-hand side

The mean, median, std and number of voxels in each ROI in every QSM image were extracted using the Segment Statistics tool in 3D-Slicer.

Further analysis and plotting was performed in MATLab [21]. In this analysis was subject susceptibility values obtained by averaging within the multiple scans of each subject and subsequently across subjects [36]. The subject susceptibility average $\bar{\chi}$ is calculated by:

$$\bar{\chi} = \frac{\sum_{i=1}^{m}(\sum_{j=1}^{n} x_{ij}/n)}{m}.$$

where n is the number of scans and m the number of subjects. Intra-subject absolute variability is assessed by measuring the within-subject standard-deviation (SD_{intra}) calculated with:

$$SD_{\text{intra}} = \sqrt{\frac{\sum_{i=1}^{m}\sigma_i^2}{m}} \text{ with } \sigma_i = \sqrt{\frac{\sum_{j=1}^{n}(x_{ij}-\bar{x_i})^2}{n}}$$

where $\bar{x_i} = \frac{\sum_{j=1}^{n} x_{ij}}{n}$ is the replicate average for each volunteer. Cross-subject variability was calculated by measuring the between-subject standard-deviation (SD_{inter}):

$$SD_{\text{inter}} = \sqrt{\frac{\sum_{i=1}^{m}\sum_{j=1}^{n}(x_{ij-x_{avg}})^2}{n \times m - 1}}$$

where $x_{avg} = \sum_{i=1}^{m}\sum_{j=1}^{n} x_{ij}/(n \times m)$ is the measurement average across subjects and scans.

Standard error of the mean (SEM) measures how far the sample mean of the data is likely to be from the true population mean. The SEM can be calculated by:

$$SEM_{ROI} = \frac{\sigma_{ROI}}{\sqrt{N}}$$

where $\sigma_{ROI} = \sqrt{\frac{(\sum_{\text{voxel}}^{\text{ROI}} \chi_{\text{voxel}} - \bar{\chi}_{\text{ROI}})}{N-1}}$ is the measured susceptibility standard deviance within a given ROI in a single QSM image, N is the number of voxel in a ROI, $\bar{\chi}$ is the average susceptibility measured within a ROI and χ_{voxel} is the susceptibility value of a single voxel in a QSM image.

As QSM images are CSF corrected, should the measured SEM in the CSF referance mask be added to the error measured in the ROI:

$$SEM_{\chi,\text{csf corrected}} = \sqrt{SEM^2_{\chi,\text{ROI}} + SEM^2_{\chi,\text{CSF mask}}}$$

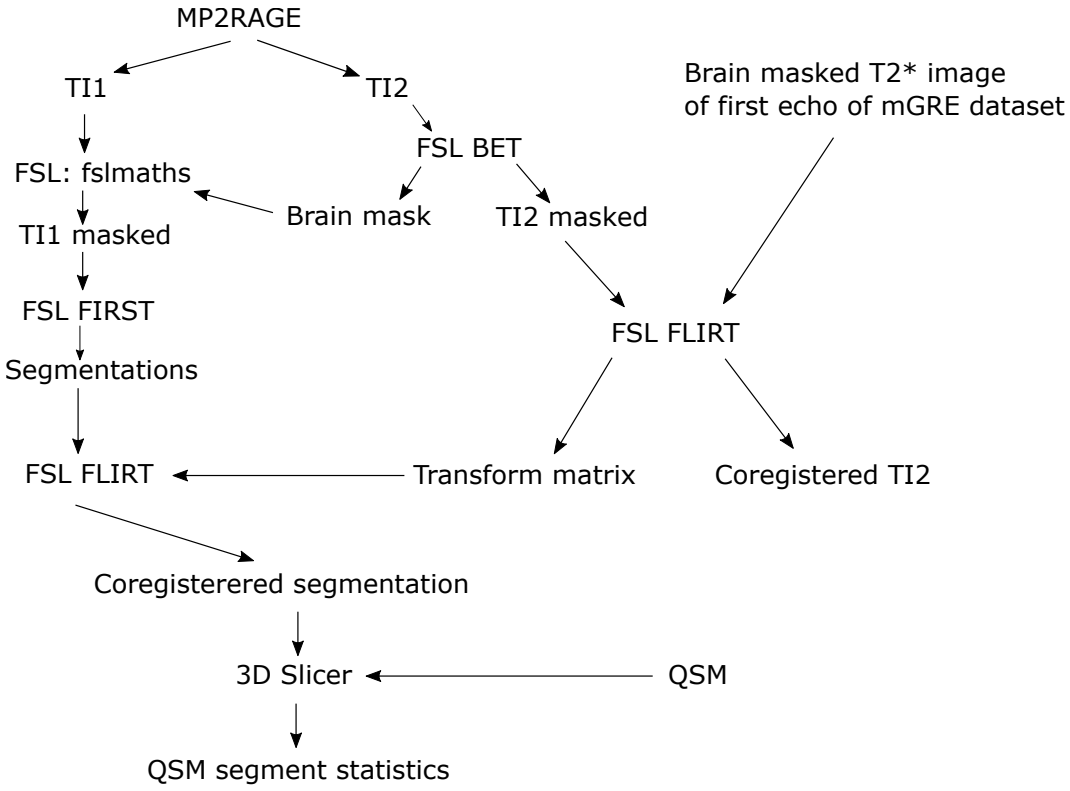

Figure 8: Segmentation flowchart

5 Results

5.1 Exclusion of volunteers

Out of 12 volunteers were 3 subjects excluded from the study. The three volunteers was excluded from this study for failing at one or several steps during the image process.

The three volunteers were excluded as a result of:

- One volunteer had a poor MP2RAGE acquisition, which showed a lot of movement artifacts. The poor quality of the T1-weighted MP2RAGE image made FSL FIRST not able to a complete segmentation for all ROIs of interest.
- The second volunteer had very small and narrow lateral ventricals. This had an impact on the second set of mGRE data, as the T2* magnitude image showed a very small identifiable ventrical volume. All measurements from this data set showed very different suseptibility values than the other two data sets of the same person, which were a lot more similar. Preliminarly is this deviation suspected to be a result of a failure in aquiring a representable CSF referanse mask, as the aquired MEDI+0 referance mask is produced by thresholding of the T2* image. As a further indication do the referance mask of the second scan contain 4104 voxels while the two other scans contain $\sim$ 12000($\pm$230) voxels. An alternative referance was considered, but that would have made the QSM images less comparable to other CSF-corrected images in the study.
- The third excluded volunteer had very asymmetrical lateral ventricals, where the left hand ventricle was a lot larger than the right hand side. This abnormality caused FSL FIRST automated segmentation to fail localizing some ROIs of interest, making the segmentation set not usable.

5.2 QSM images

Figure 9 show an example of a QSM construction using a MEDI, TKD and TGV pipeline respectively.

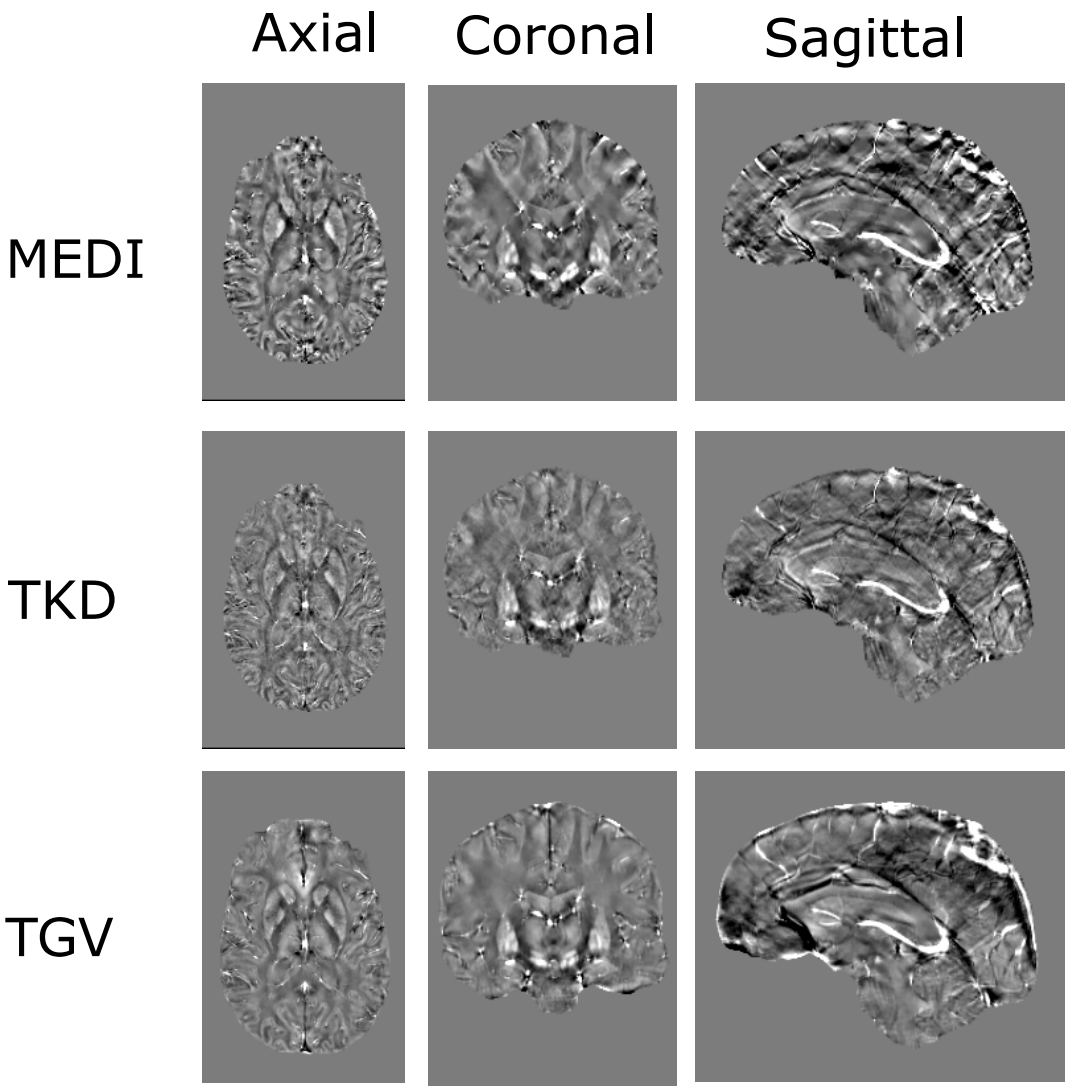

Figure 9: QSM images produced using three different QSM pipelines using a single GRE data set of one subject.

5.3 Image Segmentation

Figure 6 show a 3D representation of an example set of segmentation aquired from a T1-weighted image aquired from a MP2RAGE data set.

Figure 7 the same set of segmentation right after coregistration to a GRE data set.

5.4 Variation across different regions of interest

Figure 10 show the mean susectibility measured in each ROI, including all QSM images of across all 9 volunteers. The calculated mean ROI susceptibility averaged across all scans and subjects are tabulated in figure 2, Intersubject ROI standard deviation is tabulated in table 3 and intra-subject ROI standard deviation are tabulated in table 4. The mean standard deviation the QSM voxels within each ROI are tabulated in table 5 and the corresponding SEM are tabulated in table 6.

Mean susceptibility (ppb)			
ROI	MEDI	TKD	TGV
Left thalamus	-1.02	-1.41	2.43
Left caudate	18.49	11.53	13.67
Left putamen	11.44	7.87	8.99
Left pallidum	45.43	33.75	44.41
Left hippocampus	-3.01	-6.48	-0.38
Right thalamus	-1.46	-1.90	2.19
Right caudate	19.08	10.01	13.44
Right putamen	4.79	1.70	3.47
Right pallidum	51.39	40.34	50.73
Right hippocampus	-6.50	-7.51	-1.15

Table 2: Mean ROI susceptibility averaged across all scans and subjects.

STD across subjects (ppb)			
ROI	MEDI	TKD	TGV
Left thalamus	5.85	3.32	3.80
Left caudate	9.14	6.10	6.24
Left putamen	10.52	7.90	7.91
Left pallidum	10.51	10.11	9.61
Left hippocampus	5.80	3.22	3.99
Right thalamus	7.67	5.44	6.13
Right caudate	6.50	4.74	7.79
Right putamen	15.71	10.45	9.00
Right pallidum	5.64	3.71	4.84
Right hippocampus	10.42	7.15	7.65

Table 3: Measured cross-subject standard deviation of mean ROI susceptibility in QSM images produced by a MEDI, TKD and TGV pipeline respectively.

STD within subject (ppb)			
ROI	MEDI	TKD	TGV
Left thalamus	2.71	1.59	1.44
Left caudate	3.27	1.59	1.72
Left putamen	2.25	1.49	1.61
Left pallidum	3.94	3.27	3.17
Left hippocampus	1.76	0.89	1.15
Right thalamus	3.13	2.07	3.17
Right caudate	3.00	2.51	3.43
Right putamen	7.01	4.45	6.00
Right pallidum	2.07	1.12	1.41
Right hippocampus	2.16	1.94	2.44

Table 4: Measured within-subject standard deviation of mean ROI susceptibility in QSM images produced by a MEDI, TKD and TGV pipeline respectively.

	STD_{ROI} (ppb)		
ROI	MEDI	TKD	TGV
Left thalamus	23.	21.	21.
Left caudate	24.	20.	19.
Left putamen	28.	25.	26.
Left pallidum	45.	39.	40.
Left hippocampus	25.	20.	18.
Right thalamus	23.0	21.	21.
Right caudate	23.	20.	20.
Right putamen	28.	26.	26.
Right pallidum	40.	36.	36.
Right hippocampus	25.	20.	19.

Table 5: Standard deviation of voxel susceptibility within 10 different ROIs using three different pipelines. Pipelines using MEDI, TKD and TGV dipole inversion are considered.

	SEM_{ROI} (ppb)		
	MEDI	TKD	TGV
Left thalamus	0.12	0.03	0.020
Left caudate	0.39	0.06	0.12
Left putamen	0.62	0.10	0.12
Left pallidum	0.54	0.27	0.14
Left hippocampus	0.14	0.07	0.08
Right thalamus	0.41	0.05	0.20
Right caudate	0.12	0.10	0.31
Right putamen	0.97	0.32	0.52
Right pallidum	0.10	0.05	0.04
Right hippocampus	0.70	0.11	0.20

Table 6: Standard error of the mean (SEM) of the average susceptibility aquired from 10 different ROIs using three different pipelines. Pipelines using MEDI, TKD and TGV dipole inversion are considered.

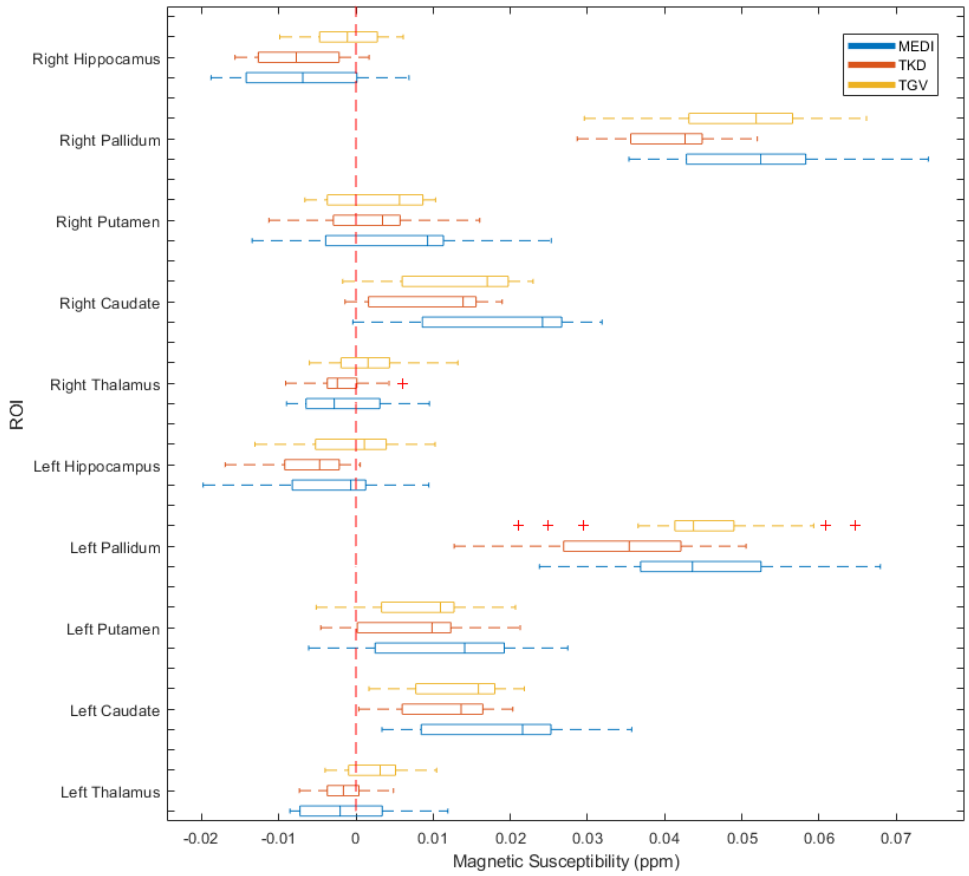

Figure 10: Measured magnetic suseptibility across 9 volunteers, each with 3 subsequent scans, across ten region of interest. Each box contains the mean segment QSM value from QSM images produced from one spesific QSM pipeline. Pipelines using MEDI (blue box), TKD (red box) and TGV (yellow box) dipole inversion are compared. The central mark in each box indicates the median, and the bottom and top edges of the box indicate the 25th and 75th percentiles, respectively. The whiskers extend to the most extreme data points not considered as outliers.

5.5 Intersubject variation

Figure 11 show a boxplot of the measured mean suseptibility in the thalamus, caudate nucleus and putamen of 9 volunteers individually, in order to show intersubject variation. An equivalent plot for the pallidum and hippocampus segments are pre-

sented in figure 12. Each box contains the measured susceptibility of three QSM images produced from three subsequent GRE scans using one QSM pipeline.

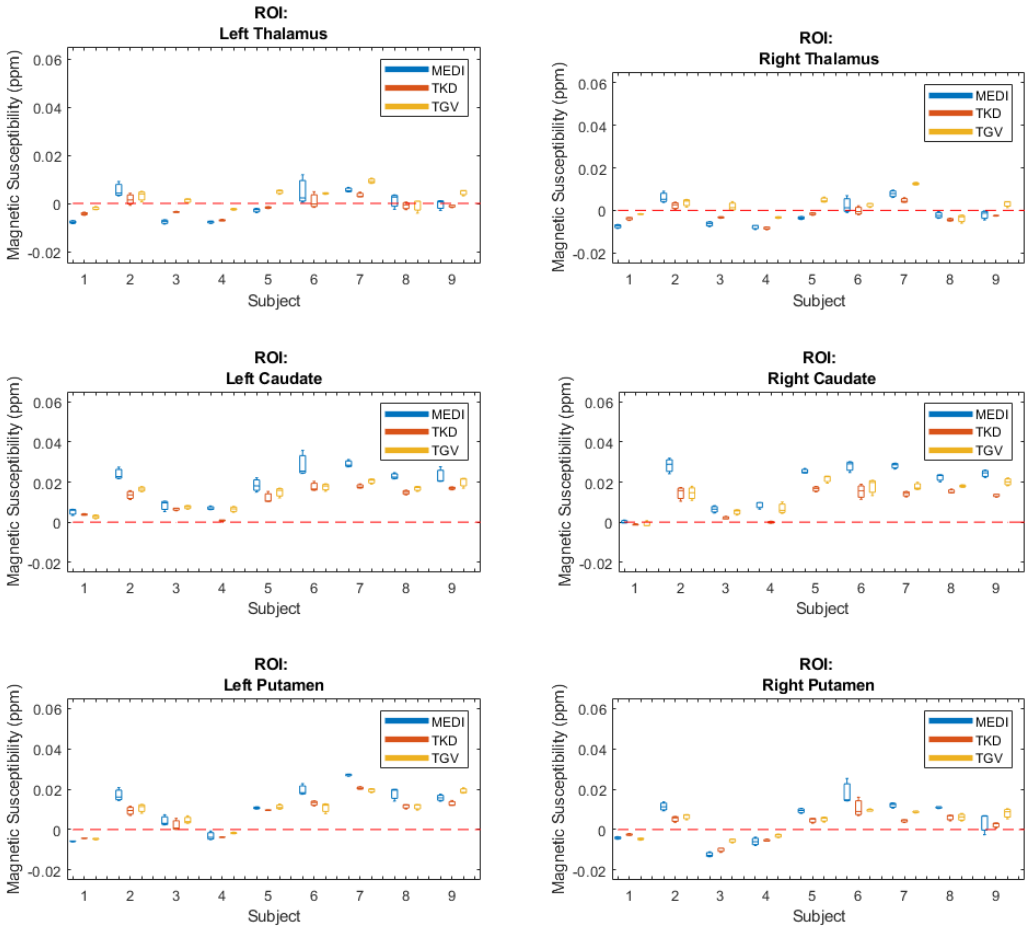

Figure 11: Mean suseptibility measured in the thalamus, caudate nucleus and putamen of 9 volunteers. Each box contains the measured susceptibility of three QSM images produced from three subsequent GRE scans using one QSM pipeline. The pipelines considered uses MEDI (blue box), TKD (red box) and TGV (yellow box) dipole inversion. The central mark in each box indicates the median, and the bottom and top edges of the box indicate the 25th and 75th percentiles, respectively. The whiskers extend to the most extreme data points not considered as outliers.

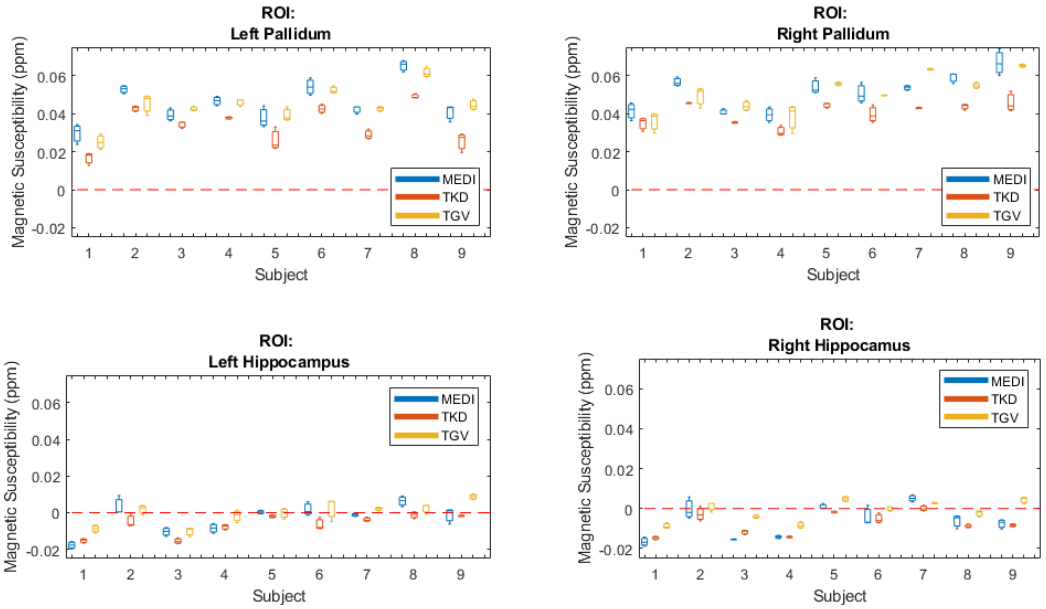

Figure 12: Mean suseptibility measured in the pallidum and hippocampus of 9 volunteers. Each box contains the measured susceptibility of three QSM images produced from three subsequent GRE scans using one QSM pipeline. The central mark in each box indicates the median, and the bottom and top edges of the box indicate the 25th and 75th percentiles, respectively. The whiskers extend to the most extreme data points not considered as outliers.

5.6 Intrasubject variation

Three scans were performed in order to study intrasubject variation. In figure 13 are mean suseptibility values aquired from all ROIs and QSMs produced from a single scan plotted against the two other scans of the same volunteer. QSM images produced using MEDI, TKD and TGV dipole inversion are all included.

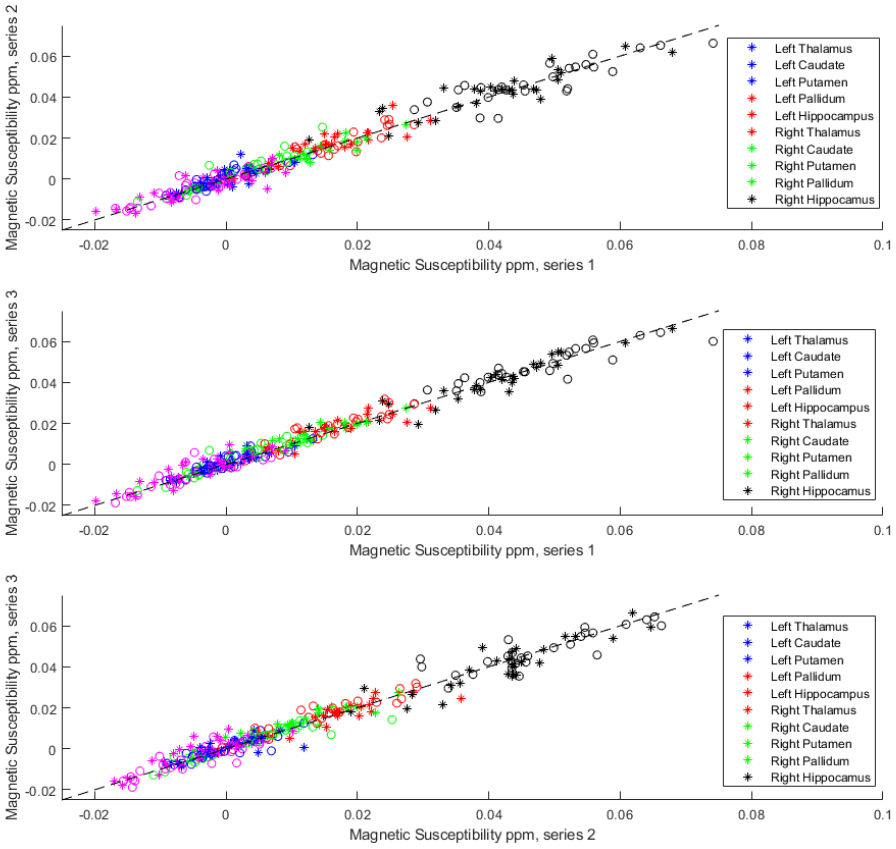

Figure 13: Segment mean suseptibility values measured in QSM images produced from three subsequent scans plotted against eachother pairwise. QSM images produced using MEDI, TKD and TGV dipole inversion are included using GRE data from 9 subjects. Segments of thalamus, caudate nucleus, putamen, pallidum and hippocampus were considered. Stars and circles indicate left- and right-hand side segmentations respectively.

5.7 Variation between different pipelines

Three different pipelines were used in this study. In figure 14 are all measured segment mean susectibilies from each of the three pipelines plotted against eachother.

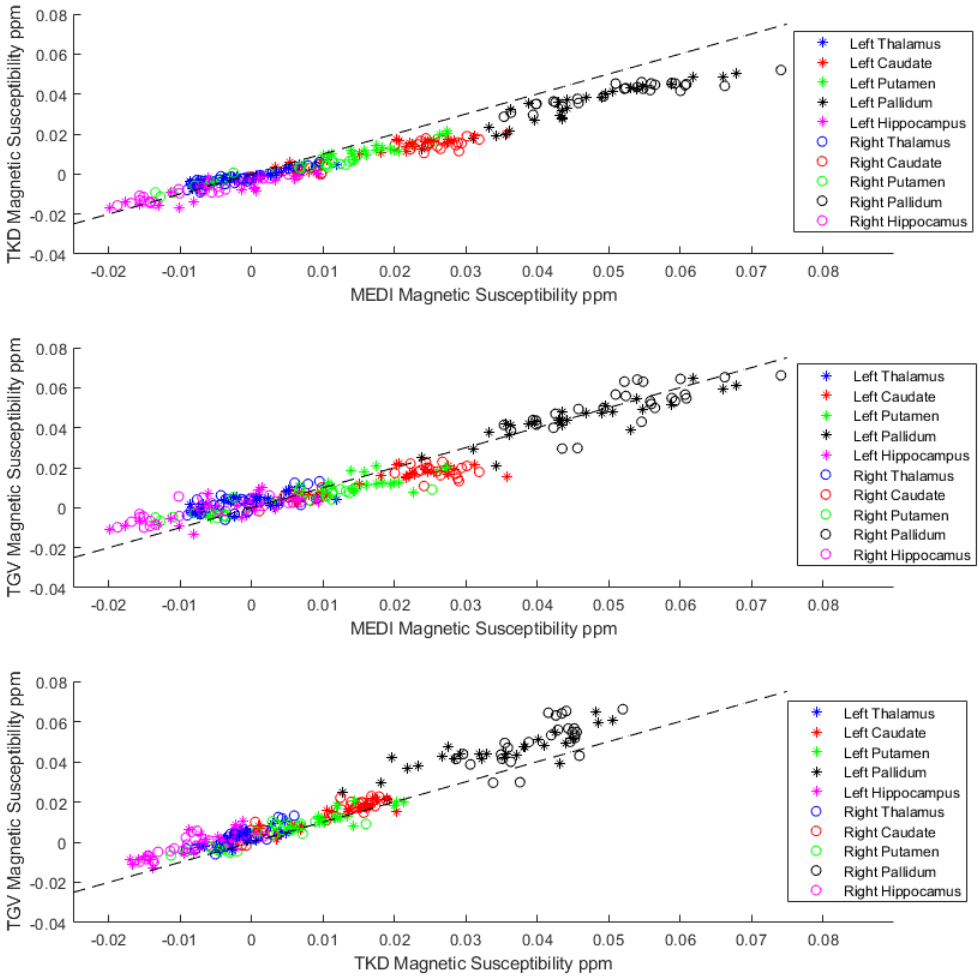

Figure 14: Segment mean suseptibility values of all QSM images produced with a specific QSM pipeline plotted against segment mean suseptibility values aquired from QSM images from an alternative pipeline. Pipelines using MEDI, TKD and TGV dipole inversion are included. Segments of thalamus, caudate nucleus, putamen, pallidum and hippocampus were considered. Stars and circles indicate left- and right-hand side segmentations respectively.

6 Discussion

6.1 QSM image quality

This study did not really focus on the optimalization of QSM image quality produced from each pipeline, but rather the consistancy of a pipeline given fixed operating parameters.

Conserning the image quality of the produsedQSM images it is apparent that the pipeline using TKD dipoleinversion produced QSMs with the lesser quality. Most of these images showed a considerable amount of streaking artifacts and lower edge contrast. Direct methods of dipole inversion, such as TKD, are to be expected [16] compare to iterative methods, such as MEDI and TGV. The oberservations done in this study collaborate that statement.

The QSM images produced using MEDI and TGV looks visualy more similar, especially in the axial plane. The TGV QSM images show some higher degree of smoothening at the expense of some edge definition compared to the MEDI images.

Even if the TKD image looks a bit crude compared to the MEDI and TGV images is noteworthy that the TKD dipole inversion algorithm is much simpler (only one parameter) and faster to run. A complete TKD pipeline had an average runtime of $\sim$ 2.5 minutes, while the QSM pipelines using MEDI and TGV had runtimes of $\sim$ 20+. With that in mind, TKD could be considered a decent alternative when runtime is a significant priority. There have been proposed methods to impose higher degree of smoothness to direct dipole inversion [37] in order to improve image quality further, but this was not considered in this study.

6.1.1 Differances in brain masking

Brain masking for all QSM images were performed FSL BET, as well as a brain mask edge erosion with a kernel size of 5 voxels prior to dipole inversion. However, in figure 9 there is an apparent differance in each implementation. By comparing the sagital QSM images in the figure there is a bright line along the outer edge of the brain in the TGV QSM image. This line is caused by phase inhomogenities outside the brain, and should be excluded by brain masking. Inclusion of such inhomogenities are a common cause of non-local image artifacs im QSM images, as the dipole inversion step is highly sensitive to local field variations. Hence a higher number of voxels should have been removed along the edge of the brain mask,especially in regards to the mask used in the TGV pipeline.

6.2 Intrasubject variation

The repeated scans on each subject was performed in order to study how the resulting QSM was prone to intrasubject variations. Figure 13 show the measured magnetic susceptibility from each of the scans plotted against the other two. In figure 13 there is some variations across on an individual level, but these variations appare to be as prominent in all three series. This could indicate that the variations are common in every acquisition. In order to study this aspect further it would be interesting to investigate if the individual variations are also present in the mGRE raw data.

Another possible source of intrasubject variations is the coregistration part of the segmentation process. In this process was a single set of segmentations coregistrated to single echo T2* magnitude image corresponding to the QSM image of interest. The quality of the T2* data is obviously important, but how small variations in T2* can affect the efficacy of the segmentation is not thoroughly investigated. Hence, it is very possible that some of the intrasubject variations are caused by inconsistant coregistration. The degree of this is however unknown and would need further study.

Another source of systematic intrasubject variations can come directly from the data acquisition. Most subjects were scanned during different sessions on different days. If would be of interest to investigate if the intrasubject variation would increase if the repeated scans of each subject were performed on separate days, or alternativly if the intrasubject variation would be reduced by scanning multiple volunteers back-to-back in a single session.

6.2.1 Effect of repositioning of volunteers and reshimming of scanner

Between the second and third scan of each volunteer we preformed a repositioning of the subject and a reshimming of the scanner. In figure 13 we can see little to no effect of this action at any of the subjects as the data corresponding to the last scan (labeled as series 3 in the figure) show no significant changes compared to the two previous scans (labeled series 1 and 2). This is promising as this makes the the process of repositioning of volunteers and reshimming of the scanner less likely to be a major systematic source of intrasubject variations.

6.3 Intersubject variation

The motivation of producing QSM images is the fact that variations in magnetic susceptibility values in QSM could be linked to biological differances in the tissue of subjects. This would be of interest as QSM values could potetially qualify as a indicator for pathology. However, as all persons in this study is considered to be healthy. Any increase in intersubject variability should only increase the threshhold of which QSM value deviations could be considered pathological.

Some natural, healthy variations are to be expected. A QSM study of 498 volunteers was performed by the University of Alberta in 2021 [38]. This study aquired QSM values from subjects with lifespans ranging from 5 to 90 years. The study observed that the average susceptibiliy increased together with the age of the subject population. Some of the ROIs studied in this work was the caudate nucleus, globus pallidus and putamen. The thalamus ROI did not increase, but showed increase in susceptibility at lower ages, reached a peak and then declined. QSM values were highest in the globus pallidus across all ages. QSM in the other three structures were similar to each other at the youngest ages, but progressively deviated with increasing age, particularly after 45–50 years. Some of the results from the 2021 University of Alberta study is presented in figure 15.

The age span in the work of this thesis was $\sim 20 - 35$ years. In this interval it is not ulikely some of the intersubject variations are age related, but a sample size of nine volunteers is too small to determine the degree it is a contribution.

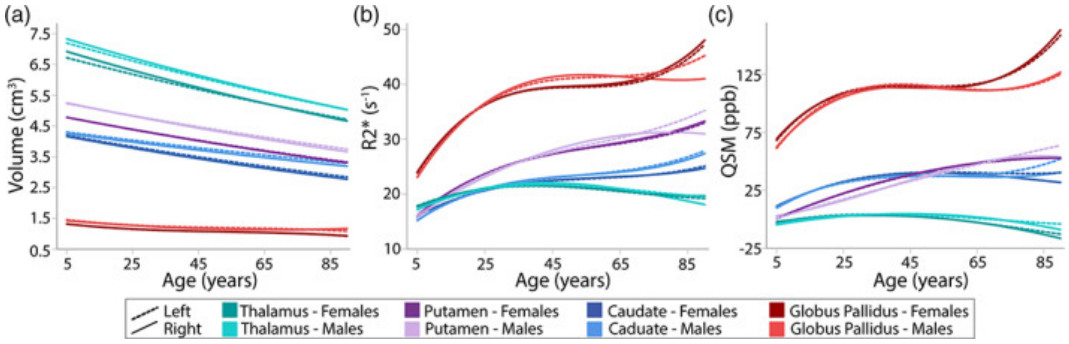

Figure 15: Best-fit curves across QSM images of 286 females and 212 males with 5–90 year lifespan. The figure plots (a) volume, (b) R2*, and (c) QSM values of the thalamus, putamen, caudate and globus pallidus, separated by sex (different shade of each color) and hemisphere (solid vs. dashed lines). The data is aquired from a separate study of QSM in deep gray matter of 498 healthy controls from 5 to 90 years [38], which were performed on a 3T scanner.

Comparing the various $\text{STD}_{\text{intrasubject}}$ in table 4 and $\text{STD}_{\text{intersubject}}$ in table 3, it shows that the intersubject STD is on average ~ 3 times larger than intrasubject across all considered ROIs and applied QSM algorithms.

6.4 Variation between different pipelines

By comparing the ROI mean susceptibility values in table 2 we see that the variation between three different QSM pipelines are of the same order of magnitude, in most ROIs, as the intrasubject deviations tabulated in table 4. The globus pallidus ROI

stand out, which show a $\sim 20\%$ lower susceptibility value in QSM images produced using the TKD pipeline compared to the other two. This behaviour is expected as as direct dipole inversion methods, such as TKD, are reported to systematically underestimate magnetic susceptibilities [16]. The underestimation of TKD is even more apparent in figure 14, which show a systematic lower mean susceptibility estimation in TKD data across all ROIs, especially in the pallidum and caudate nucleus ROIs. This trend is seen in figure 10 aswell.

Excluding the TKD data result a cross-pipeline standard deviation between the MEDI and TGV data is about half of the magnitude of the equivalent $STD_{\text{intrasubject}}$.

Comparing only MEDI and TGV in figure 14 we see a higher susceptibility estimation in cuadate and putamen for the MEDI data and a higher susceptibility estimations in the pallidum and thalamus ROIs. The length of the boxes, indicating the 25th and 75th percentile, in figure 11 and 12 indicate a lower intra subject variation in the TGV data compared to the MEDI data. A similar trend can be seen in figure 10 which indicate a lower intersubject variation aswell.

One possible origin of the higher intra- and inter-subject variations in the MEDI images is the QSM weight step in the SEPIA toolbox. This step is essensially an additional voxel-by-voxel QSM scaling step, which the TGV algorithm does not have.

The largest source of variations is the parameters in which each pipeline used were mostly their respective default settings, and are probably sub-optimal in regards to measuring the exact susceptibility in each ROI. However, by leaving the variables fixed makes the variations in the resulting QSM images solely dependent on the raw data. Making the QSM variations an indication of the viability of each pipeline.

6.5 ROI specific susceptibility variations

A study of reliability of ultra-high field T2* MRI at 7T, a part of the UK7T Network's "Travelling Heads" extensive study, was published in 2020 [36]. In this study was ten healthy volunteers were scanned with harmonised single- and multi-echo T2*-weighted gradient echo pulse sequences. The participants were scanned five times at each site and once at each of four other sites. The five sites had $1\times$ Philips, $2\times$ Siemens Magnetom, and $2\times$ Siemens Terra scanners. QSM images were computed with a Multi-Scale Dipole Inversion (MSDI) algorithm [39]. The published litterature susceptibility values as well at their own calulated susceptibilitues in ROIs of the caudate nucleus, putamen and globus pallidusare presented in figure 16.

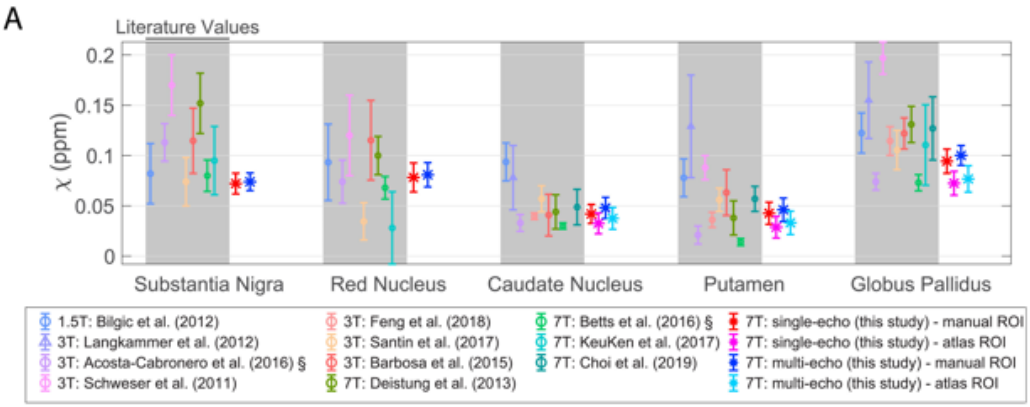

Figure 16: Mean and standard deviation literature values of QSM. Shaded regions correspond to literature data. The data plotted in the unshaded area are gathered from a UK7T study, which included a study of multi-center, multi-vendor reproducibility of 7T QSM.Their multi-echo QSM images were calculated with data from mGRE data sets with eight echoes. The plot is exported from an article from the UK7T study [36].

The segment susceptibilities reported in the multi-center study in figure 16 show slightly lower susceptibility values compared to manually segmented ROIs. This is suspected to be a result of inaccuracies in the atlas segmentations allows an inclusion of voxels with negative susceptiblity outside the actual ROI. Inclusion of negative voxels can potentially reduce the average magnetic susceptibility in a given segment.

The average ROI susceptibility measured in this work is presented in figure 10. Compared to the susceptibility values from the UK7T study in figure 16 it is obviou that the susceptibilities obtained in this study is much lower for the caudate, putamen and pallidum ROIs. Out of these three ROIs can only pallidum and the caudate nucleus be sufficiently differanciated from zero. The relative increase between each of these three ROIs appare to fall within the relative range of the litterature values in figure 16. Big differances in the relative susceptiblity would indicate that there is a significant scaling issue in the QSM pipeline.

However, the largest issue is a there is a significant fixed offset between the QSM values in this study and the litterature values. An error in the zero-referancing step is more than likely to have contributed to this offset. However, as the unreferanced QSM data is not available for the SEPIA data in this study, since only CSF referanced images are produced with the applied parameters.

Hence, zero referancing should not be integrated into in dipole inversion step of QSM, as it would make it easier to monitor how much is corrected during the zero referancing process. Instead this step should be a part of the QSM post-proscessing

making both the unreferanced and referanced QSM image available for analysis.

Another interesting trend in table 4, 3 and 6 is that the ROIs on the right-hand side show a systematic higher STD and SEM than the left-hand side. This implies that the measured QSM values are systematically less uniform on the right-hand side compared to the left. This can be random, but can also be caused by a instrument inconsistencies during the data acquisition. Such inconsistencies could include inhomogen scanner magnetic field, asymetric coil-sentivity or asymetric head placement within the coil to name some.

6.6 Choice of referance region

As mentioned in section 6.5 are the method of zero referancing a likely source of error in this work. This is likely a result of how the MEDI+0 uses thresholding of the T2* magnitude image to produce a CSF referance mask. The method is heavily dependent on easily segmentable lateral ventricals in T2* magnitude images. This is not necessarily universally available.

In this study alone was one out of twelve initial volunteers excluded due to poor CSF segmentation using the MEDI+0 algorithm. This individual had lateral ventricals with a very low total volume. The data from the three successive scans resulted in three QSM images with widely different susceptibility values using all three pipelines. A consideration of other referance regions is needed. Either other parts of the brain should be considered, or inclusion of volumes of CSF outside of the lateral ventricals.

The QSM data from the volunteers that could be zero referanced using the MEDI+0 algorithm would probably benefit further improvements on the CSF referance mask. The primary one being an additional mask erosion along the referance mask in order to avoid any unreliable voxels along the mask boundary.

It is also important to mention that there is a number of medical conditions can alter the magnetic susceptibility of CSF itselv. Hemmorages and ventrical calcifications can for example cause a positive or negative susceptibility shift in CSF, which would cause an equivalent shift in the entire QSM image in cases CSF are used for zero referancing. Hence, alternative referance regions should be considered and made available, even if CSF is considered as the prime referance region.

6.7 Segmentation and coregistration

Most of the difficulties concerning both the automated segmentation and coregistration arise from the increased image resolution of 7T data. Most conventional MRI software available which are developed for clinical use. As most common clinical MRI scannes uses magnetic fields at 1.5 or 3T. Scanners with a lower main magnetic field generally produce images at a lower resolution, compared to 7T. This makes conventional MR software, which are tailored to process MR images of the

lower resolution of clinical scanners, more likely to struggle to perform thresholding and resampling technices while maintaining the higher resolution of MR images ultra-high field scanners.

Coregistration between the T1 and QSM images with FSL FLIRT where attempted directly, as T1 images were used for segmentation. This was without success. Coregistration of QSM to T1 images resulted in blurred QSM images, while coregistration of T1 to QSM resulted in blurred T1 images which could not be segmented by FSL FIRST.

The MP2RAGE TI2 and T2* images origin from the same aquisition data as the T1 and T2* images respectively, but show a more similar image contrast to each other. This made the coregistration of the TI2 and T2* images much more consistant than the alternatives. Coregistration of TI2 to T2* yield a transformation matrix which can be applied to segmentations from the original T1 images. The coregistrated segmentations can then be applied to the corresponding QSM image matixes. There is resampling issues for the segmentations aswell, but it is far easier to correct errors created in a binary mask, than in a complex QSM image.

All of these issues and additional steps occur because of the need of two separate acquisition sequences, one to produce the QSM image and another to provide the basis of the analysis of the QSM image. These steps could have been avoided by performing the tissue segmentation directly in the QSM image, either by automatic of manual segmentation.

It is hard to determine if the segmentation process itself is reprocuable as only one set of segmentation is considered in this study, as only one T1-weighted MR image was aquired. Optimaly should an additional T1 image be obained for each individual in order to check for within subject variations of the T1-weighted images.

Manual segmentations should have been included in this study, which could could function as a ground truth segmentation. Manual segmentations in both T1 and directly in QSM would be of interst, in order to distinguish variations which occur during coregistration of T1-segmentations.

Using tools like FSL FIRST also limits the available segmetations to tissues which is only easily segmented in T1 images. Deep brain tissues like the red nucleus and substantia nigra for example are examples of tissue with relative low T1 contrast, but high contrast in QSM images. A comparison of the differancein contrast of the red nucleus in T1 and TGV QSM is illustrated in figure 17.

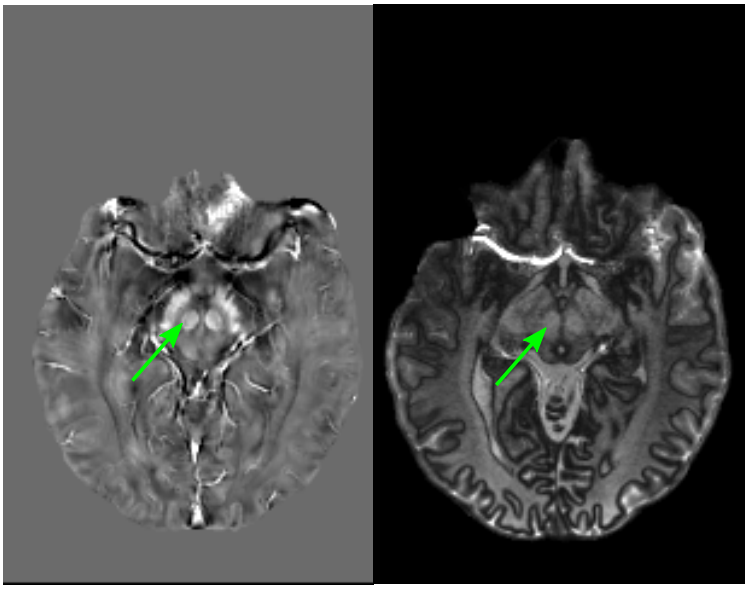

Figure 17: TGV QSM image and a T1 weighed MP2RAGE image aquired from the same subject. The arrow indicate the location of the left red nucleus.

Reproducibility of segmentations is arguably just as important as the the reproducibility of the QSM images themselves, as the ability to compare QSM images are dependent on the quality of the segmentations.

6.8 QSM weights

The SEPIA application of a weight map in the QSM step add an image quality constraint to the final QSM image. The weights are inversly proportional to the noise in the image. The signal to noise ratio decreases with TE, which will make contribution of echo images at longer echo times be weighted less to the final QSM.

QSM weighting is an aspect which potetially separates TGV QSM images from the SEPIA images, as the single echo TGV QSM images are not weighted. The TGV QSM images is only scaled $\propto \frac{1}{TE}$ after dipole inversion. This scaling is sensible in regards to signal to noice ratios at longer echo times, but might be a bit crude as the image quality not directly considered. Hence, two single echo TGV QSM images with different quality, but equal TE would be weighted the same in the TGV pipeline used in this work, which would be sub-optimal.

There are a number of approaches to echo combination in the TGV pipeline that would be of interest in further studies.

The first would be to try to combine all mGRE echo phase images into a combined phase image as a step in the pre-QSM-processing, similar to what the SEPIA toolbox does. Only having a single phase image to process can potentially simplify the post-

processing as only one QSM image are produced in the pipeline. The scaling step in the TGV algorithm can be easily bypassed by not providing the algorith with an echo time, this will invoke a scaling factor of 1 by default. The final scaling can be done done by calculating a scaling factor specific to the applied mGRE sequence.

6.9 Further work

For further work should the reproducibility of segmentations take priority over the reproducibility of the QSM image themselves, as it is not possible to relighably compare QSM images without very relighable segmentations.

In this respect should methods of automated segmentations methods using QSM images as input be of interest. Such approaches to automated segmentation would be of special interest as these methods are less likely to be dependent of secondary scan sequenses and the segments can be applied directly to the QSM image without alterations. If a reliable automated segmentation method is not avaliable, the manual segmentation should be considered.

A study of reproducible methods of coregistration of 7T data would also be of interest, as coregistration is essencial in any study of medical imaging outside the scope of QSM specifically.

7 Conclusion

In conclusion does the study indicate that intersubject factors appear to have by far the most prominent effect on the reproducibility of quantitative susceptibility maps. Some variation is expected, as many factors may influence a tissues magnetic susceptibility. Further more, there was observed a varied degrees of intrasubject variations among the scanned subjects. Larger variations were linked to lower quality of the raw data. As low quality raw data not only affect the quality of the QSM images, but also affect the ability to perform automated segmentation and coregistration of images.

Intrasubject variation is lower than intersubject variations, with intersubject STD being on average a third of the magnitude of the intrasubject STD. Variation between the applied pipelines are of a similar magnitude as the intrasubject variation, but this can most likely be minimized further by improving each pipeline individually.

In regards to the three different pipelines themselves, only TKD would not be recommended for further studies at this method showed both poorer image quality and had a systematic underestimation of QSM values. Both MEDI and TGV showed promising variations in regards to intra- and intersubject variation for within-site studies. A more dependable method of setting QSM referance is needed in order to do any future cross-site studies.

Reproducibility of segmentations is arguably just as important as the the reproducibility of the QSM images themselves, as the ability to compare QSM images are dependent on the quality of the segmentations.

References

[1] Mechelle M. Lewis, Guangwei Du, Michal Kidacki, Nisargkumar Patel, Michele L. Shaffer, Richard B. Mailman, and Xuemei Huang. Higher iron in the red nucleus marks parkinson's dyskinesia. *Neurobiology of aging*, 34(5):1497–1503, May 2013. 23177595[pmid].

[2] Michael Khalil, Christian Langkammer, Alexander Pichler, Daniela Pinter, Thomas Gattringer, Gerhard Bachmaier, Stefan Ropele, Siegrid Fuchs, Christian Enzinger, and Franz Fazekas. Dynamics of brain iron levels in multiple sclerosis. *Neurology*, 2015.

[3] Stefan Ropele and Christian Langkammer. Iron quantification with susceptibility. *NMR in Biomedicine*, 30(4):e3534, 2017. e3534 NBM-15-0293.R1.

[4] Jeff H. Duyn and John Schenck. Contributions to magnetic susceptibility of brain tissue. *NMR in Biomedicine*, 30(4):e3546, 2017. e3546 NBM-15-0325.R1.

[5] M. Khalil, C. Langkammer, A. Pichler, D. Pinter, T. Gattringer, G. Bachmaier, S. Ropele, S. Fuchs, C. Enzinger, F. Fazekas, and et al. Dynamics of brain iron levels in multiple sclerosis: A longitudinal 3t mri study. *Neurology*, 84(24):2396–2402, 2015.

[6] Govind B. Chavhan, Paul S. Babyn, Bejoy Thomas, Manohar M. Shroff, and E. Mark Haacke. Principles, techniques, and applications of t2*-based mr imaging and its special applications. *RadioGraphics*, 29(5):1433–1449, 2009. PMID: 19755604.

[7] Dual/multi-echo gre. *MRIquestions*, 2022.

[8] José P. Marques, Tobias Kober, Gunnar Krueger, Wietske van der Zwaag, Pierre-François Van de Moortele, and Rolf Gruetter. Mp2rage, a self bias-field corrected sequence for improved segmentation and t1-mapping at high field. *NeuroImage*, 49(2):1271–1281, 2010.

[9] Woojin Jung, Steffen Bollmann, and Jongho Lee. Overview of quantitative susceptibility mapping using deep learning: Current status, challenges and opportunities. *NMR in Biomedicine*, n/a(n/a):e4292. e4292 NBM-19-0283.R1.

[10] Ferdinand Schweser, Simon Daniel Robinson, Ludovic de Rochefort, Wei Li, and Kristian Bredies. An illustrated comparison of processing methods for phase mri and qsm: removal of background field contributions from sources outside the region of interest. *NMR in Biomedicine*, 30(4):e3604, 2017. e3604 NBM-15-0314.R2.

[11] Ferdinand Schweser, Andreas Deistung, Berengar Wendel Lehr, and Jürgen Rainer Reichenbach. Quantitative imaging of intrinsic magnetic tissue properties using mri signal phase: An approach to in vivo brain iron metabolism? *NeuroImage*, 54(4):2789–2807, 2011.

[12] Wei Li, Bing Wu, and Chunlei Liu. Quantitative susceptibility mapping of human brain reflects spatial variation in tissue composition. *NeuroImage*, 55(4):1645–1656, 2011.

[13] QSM Challenge 2.0 Organization Committee, Berkin Bilgic, Christian Langkammer, José P. Marques, Jakob Meineke, Carlos Milovic, and Ferdinand Schweser. Qsm reconstruction challenge 2.0: Design and report of results. *Magnetic Resonance in Medicine*, 86(3):1241–1255, 2021.

[14] Tian Liu, Jing Liu, Ludovic de Rochefort, Pascal Spincemaille, Ildar Khalidov, James Robert Ledoux, and Yi Wang. Morphology enabled dipole inversion (medi) from a single-angle acquisition: Comparison with cosmos in human brain imaging. *Magnetic Resonance in Medicine*, 66(3):777–783, 2011.

[15] Yi Wang and Tian Liu. Quantitative susceptibility mapping (qsm): Decoding mri data for a tissue magnetic biomarker. *Magnetic Resonance in Medicine*, 73(1):82–101, 2015.

[16] Andreas Deistung, Ferdinand Schweser, and Jürgen R. Reichenbach. Overview of quantitative susceptibility mapping. *NMR in Biomedicine*, 30(4):e3569, 2017. e3569 NBM-15-0326.R2.

[17] Zhe Liu, Pascal Spincemaille, Yihao Yao, Yan Zhang, and Yi Wang. Medi+0: Morphology enabled dipole inversion with automatic uniform cerebrospinal fluid zero reference for quantitative susceptibility mapping. *Magnetic Resonance in Medicine*, 79(5):2795–2803, 2018.

[18] Sam Wharton, Andreas Schäfer, and Richard Bowtell. Susceptibility mapping in the human brain using threshold-based k-space division. *Magnetic Resonance in Medicine*, 63(5):1292–1304, 2010.

[19] Christian Langkammer, Kristian Bredies, Benedikt A. Poser, Markus Barth, Gernot Reishofer, Audrey Peiwen Fan, Berkin Bilgic, Franz Fazekas, Caterina Mainero, and Stefan Ropele. Fast quantitative susceptibility mapping using 3d epi and total generalized variation. *NeuroImage*, 111:622–630, 2015.

[20] Korbinian Eckstein, Barbara Dymerska, Beata Bachrata, Wolfgang Bogner, Karin Poljanc, Siegfried Trattnig, and Simon Daniel Robinson. Computationally efficient combination of multi-channel phase data from multi-echo acquisitions (ASPIRE). *Magn Reson Med*, 79(6):2996–3006, October 2017.

[21] The Mathworks. Matlab (r2017b). 2020.

[22] Y. Wang. Sepia. 2022.

[23] Y. Wang. Quantitative susceptibility mapping. 2022.

[24] Jing Liu, Tian Liu, Ludovic de Rochefort, James Ledoux, Ildar Khalidov, Weiwei Chen, A. John Tsiouris, Cynthia Wisnieff, Pascal Spincemaille, Martin R. Prince, and Yi Wang. Morphology enabled dipole inversion for quantitative susceptibility mapping using structural consistency between the magnitude image and the susceptibility map. *NeuroImage*, 59(3):2560–2568, Feb 2012. 21925276[pmid].

[25] NITRC. Mricron. 2019.

[26] Xiangrui Li, Paul S. Morgan, John Ashburner, Jolinda Smith, and Christopher Rorden. The first step for neuroimaging data analysis: Dicom to nifti conversion. *Journal of Neuroscience Methods*, 264:47–56, 2016.

[27] Mark Jenkinson, Christian F. Beckmann, Timothy E.J. Behrens, Mark W. Woolrich, and Stephen M. Smith. Fsl. *NeuroImage*, 62(2):782–790, 2012. 20 YEARS OF fMRI.

[28] Simon Daniel Robinson, Kristian Bredies, Diana Khabipova, Barbara Dymerska, José P. Marques, and Ferdinand Schweser. An illustrated comparison of processing methods for mr phase imaging and qsm: combining array coil signals and phase unwrapping. *NMR in Biomedicine*, 30(4):e3601, 2017. e3601 NBM-15-0313.R2.

[29] Marvin A. Schofield and Yimei Zhu. Fast phase unwrapping algorithm for interferometric applications. *Opt. Lett.*, 28(14):1194–1196, Jul 2003.

[30] C. Liu. Sti suite. 2022.

[31] Brian Patenaude, Stephen M Smith, David N Kennedy, and Mark Jenkinson. A bayesian model of shape and appearance for subcortical brain segmentation. *Neuroimage*, 56(3):907–922, February 2011.

[32] Andriy Fedorov, Reinhard Beichel, Jayashree Kalpathy-Cramer, Julien Finet, Jean-Christophe Fillion-Robin, Sonia Pujol, Christian Bauer, Dominique Jennings, Fiona Fennessy, Milan Sonka, John Buatti, Stephen Aylward, James V. Miller, Steve Pieper, and Ron Kikinis. 3d slicer as an image computing platform for the quantitative imaging network. *Magnetic Resonance Imaging*, 30(9):1323–1341, 2012. Quantitative Imaging in Cancer.

[33] M Jenkinson and S Smith. A global optimisation method for robust affine registration of brain images. *Med Image Anal*, 5(2):143–156, June 2001.

[34] Douglas N Greve and Bruce Fischl. Accurate and robust brain image alignment using boundary-based registration. *Neuroimage*, 48(1):63–72, June 2009.

[35] M Jenkinson and S Smith. A global optimisation method for robust affine registration of brain images. *Med Image Anal*, 5(2):143–156, June 2001.

[36] Catarina Rua, William T. Clarke, Ian D. Driver, Olivier Mougin, Andrew T. Morgan, Stuart Clare, Susan Francis, Keith W. Muir, Richard G. Wise, T. Adrian Carpenter, Guy B. Williams, James B. Rowe, Richard Bowtell, and Christopher T. Rodgers. Multi-centre, multi-vendor reproducibility of 7t qsm and r2* in the human brain: Results from the uk7t study. *NeuroImage*, 223:117358, 2020.

[37] Berkin Bilgic, Itthi Chatnuntawech, Audrey P. Fan, Kawin Setsompop, Stephen F. Cauley, Lawrence L. Wald, and Elfar Adalsteinsson. Fast image reconstruction with l2-regularization. *Journal of Magnetic Resonance Imaging*, 40(1):181–191, 2014.

[38] Sarah Treit, Nashwan Naji, Peter Seres, Julia Rickard, Emily Stolz, Alan H. Wilman, and Christian Beaulieu. R2* and quantitative susceptibility mapping in deep gray matter of 498 healthy controls from 5 to 90years. *Human Brain Mapping*, 42(14):4597–4610, 2021.

[39] Julio Acosta-Cabronero, Carlos Milovic, Hendrik Mattern, Cristian Tejos, Oliver Speck, and Martina Callaghan. A robust multi-scale approach to quantitative susceptibility mapping. *NeuroImage*, 183, 07 2018.